H$_2$ active jets in the near IR as a probe of protostellar evolution *

A. Caratti o Garatti[1,2], T. Giannini[1], B. Nisini[1] and D. Lorenzetti[1]

[1] INAF - Osservatorio Astronomico di Roma, via Frascati 33, I-00040 Monte Porzio (Italy)
[2] Università degli Studi di Roma "Tor Vergata" - Dipartimento di Fisica, via della Ricerca Scientifica 1, I-00133 Roma (Italy) e-mail: `caratti,giannini,nisini,dloren@mporzio.astro.it`

Abstract. We present an in-depth near-IR analysis of a sample of H$_2$ outflows from young embedded sources to compare the physical properties and cooling mechanisms of the different flows. The sample comprises 23 outflows driven by Class 0 and I sources having low-intermediate luminosity. We have obtained narrow band images in H$_2$ 2.12 μm and [Fe II] 1.64 μm and spectroscopic observations in the range 1-2.5 μm. From [Fe II] images we detected spots of ionized gas in ∼74% of the outflows which in some cases indicate the presence of embedded HH-like objects. H$_2$ line ratios have been used to estimate the visual extinction and average temperature of the molecular gas. A_v values range from ∼2 to ∼15 mag; average temperatures range between ∼2000 and ∼4000 K. In several knots, however, a stratification of temperatures is found with maximum values up to 5000 K. Such a stratification is more commonly observed in those knots which also show [Fe II] emission, while a thermalized gas at a single temperature is generally found in knots emitting only in molecular lines. Combining narrow band imaging (H$_2$, 2.12 μm and [Fe II], 1.64 μm) with the parameters derived from the spectroscopic analysis, we are able to measure the total luminosity of the H$_2$ and [Fe II] shocked regions (L_{H_2} and $L_{[Fe II]}$) in each flow. H$_2$ is the major NIR coolant with an average $L_{H_2}/L_{[Fe II]}$ ratio of ∼10^2. We find that ∼83% of the sources have a L_{H_2}/L_{bol} ratio ∼0.04, irrespective of the Class of the driving source, while a smaller group of sources (mostly Class I) have L_{H_2}/L_{bol} an order of magnitude smaller. Such a separation reveals the non-homogeneous behaviour of Class I, where sources with very different outflow activity can be found. This is consistent with other studies showing that among Class I one can find objects with different accretion properties, and it demonstrates that the H$_2$ power in the jet can be a powerful tool to identify the most active sources among the objects of this class.

Key words. stars: circumstellar matter – ISM: jets and outflows – ISM: kinematics and dynamics – ISM: lines

1. Introduction

Matter flows emitted from young stellar objects (YSOs) are manifestations commonly observed during all the phases of Pre-Main Sequence evolution: from the early accretion phase (Class 0), which lasts a relatively short time ($\sim 10^4$ yrs, for a low mass YSO), to the final contraction toward the Main Sequence (Class II and III, $\sim 10^7$ yrs). According to low mass star formation models, mass accretion and ejection rates ($\dot{M}_{acc}$, $\dot{M}_{out}$) are expected to be strictly related, because a significant fraction of the infalling material is ejected by the accretion disk. The efficiency of such a coupling, however, has to necessarily decrease while the evolution proceeds. Therefore the outflow/jet properties are expected to remarkably change with time and their study offers both direct and indirect clues to understand the processes related to protostellar evolution. In addition, several issues can be addressed by

systematic observations of jets since: (*i*) they signal the presence of strongly embedded driving sources, often invisible up to far IR wavelengths; (*ii*) their shape may help to reconstruct the star/disk rotation; (*iii*) they have dynamical and chemical effects on the closeby interstellar material; (*iv*) at the same time, they are also influenced by the properties of such material.

Since bipolar and collimated jets are easily observed from the ground over a wide range of frequencies, large imaging and spectroscopical data-bases have been accumulated by various groups. Our group, in particular, has gathered, over the last five years, a large spectroscopical data set in the near IR (1–2.5 μm), complemented with a considerable amount of high-resolution imaging data ([Fe II], H$_2$), on a sample of active H$_2$ outflows from both Class 0 and Class I sources. The material collected so far has allowed us to clarify specific aspects of the protostellar jets physics, such as the identification of the crucial spectral range for the study of the H$_2$ excitation conditions (Giannini et al., 2002); the role of [Fe II] as a diagnostic

tool of embedded atomic jets (Nisini et al., 2002b); the observational tests of state-of-art shock models (Giannini et al., 2004; McCoey et al., 2004; Giannini et al., 2005b). Moreover, near IR spectroscopy allowed us to investigate the properties of H_2 jets in individual star-forming regions (IC1396; Nisini et al., 2001), (Vela Molecular Ridge; Caratti o Garatti et al., 2004; Giannini et al., 2001, 2005a; Lorenzetti et al., 2002). Here we use our data-base to derive more general properties on the IR activity of jets from young stars. This has been done complementing our published data with new observations focused mainly on the youngest Class 0 sources.

The main aim of this study is to reveal any systematic difference in the derived physical parameters which can be attributed to an effect of the evolution in both the intrinsic jet properties and in the way the jet interacts with the ambient medium. In addition, we want to define if any relationship exists between the total IR cooling of the outflows and the evolutionary status of the driving source. Indeed, several authors (see e. g. Cabrit & Bertout, 1992; Bontemps et al., 1996; Saraceno et al., 1996; André et al., 2000; Nisini et al., 2002a) have observationally shown that during the first stages of protostellar evolution a correlation exists between different tracers of the outflow activity and the source bolometric luminosity, which is believed to be largely dominated by the accretion luminosity ($L_{bol} \approx L_{acc} = GM_* \dot{M}_{in}/R_*$).

In the near IR the jet shocked excited regions mainly cool through H_2 quadrupole transitions, therefore the bright ro-vibrational lines in that range represent a suitable shock tracer which can be used to evaluate the molecular hydrogen luminosity (L_{H_2}) of the outflow. Due to its very rapid cooling, H_2 is more suitable to probe shock excitation and gas cooling than the CO lines which can only give a time-integrated response (see e. g. Smith, 2002). The empirical classification of early protostellar evolution by means of the H_2 luminosity of the emitted jets has recently attracted much attention in different works (Stanke, 2000; Smith, 2002; Froebrich et al., 2003; O'Connell , 2005), where the simplified assumption was adopted that the total H_2 luminosity is derivable from the $2.122\,\mu m$ (1-0S(1)) line luminosity. In the following, the validity of such an assumption as well as the most critical aspects in deriving a reliable value of L_{H_2} will be also reviewed.

The structure of the paper is the following: in Sect.2 we define the investigated sample of jets and associated YSOs with their parameters; in Sect.3 our NIR observations are presented; in Sect.4 we derive, for each jet, the physical quantities from the molecular and ionic components; in Sect.5 a discussion is presented in terms of jet properties vs. luminosity of the central object. Our conclusions are summarized in Sect.6. Finally, in Sect.7 (Appendix) the detailed results on any individual star forming region are reported.

2. The investigated sample

The investigated sample of H_2 jets is presented in Table 1. The driving selection criterion is the occurrence of jet activity in the near IR: for each selected source an IR jet has been detected in previous H_2 2.12 μm narrow band imaging at a sensitivity level adequate to perform low resolution near IR spectroscopy with currently available instrumentation. The second criterion is the existence of a recognized exciting source whose bolometric luminosity is well ascertained and typical of low to intermediate mass young objects ($0.2L_\odot \leq L_{bol} \leq 640L_\odot$). An important consequence of our criteria is that the selected targets are associated only with Class 0 and I driving sources, while objects belonging to more evolved classes remain unselected. Thus the jets exhibiting strong enough H_2 emission are those related to deeply embedded protostars. In particular, our sample is constituted by 23 H_2 active jets, whose driving sources are distributed as 12 Class 0, 9 Class I and 2 intermediate Class (0/I), according to the literature (see e. g. Froebrich, 2005). Table 1 lists the exciting source and its correlated HH, the coordinates of the exciting source, its evolutionary Class, bolometric luminosity and distance. The given range of L_{bol} for each source stems from different determinations given in the literature. All the targets belong to nearby star forming regions ($\leq 800\,pc$), with the exception of $IRAS07180$–2356 located at $1500\,pc$.

Not all the outflows of the sample show a clear bipolar structure, being sometimes located in crowded regions where jets from different YSOs are present. In Table 1 column 3, an asterisk indicates those outflows (14 out of 23) that exhibit a clear morphology and all the observed H_2 knots can be associated with the same driving source (see also Sec. 4.1, 4.3 and the Appendix).

3. Observations and data reduction

3.1. Imaging

The observations presented in this paper were collected during several runs between 1999 and 2005, at four different telescopes, namely ESO-VLT and ESO-NTT (Chile), Telescopio Nazionale Galileo (TNG) (Canary Islands-Spain) and AZT-24 (Campo Imperatore-Italy) (see Table 2). In addition, data from the ESO science archive facility[1] have been retrieved for HH24, BHR71 and IRAS18273+0113.

We used narrow band filters centered on the H_2 (2.12 μm) and [Fe II] (1.64 μm) lines to detect both molecular and ionic emission along the outflows. Additional broad band (H and K) or narrow band imaging at nearby wavelength positions have been gathered to remove the continuum. Table 3 summarizes the characteristics of the different near IR cameras used for our observations.

---

[1] http://archive.eso.org/

Table 1. The investigated sample

Id	Source	Associated HH	α(2000.0) (^{h} ^{m} ^{s})			δ(2000.0) ($^\circ$ $'$ $''$)			Class	L_{bol} ($L_\odot$)	Ref.	D (pc)
1	L1448-MM	-	03	25	38.8	30	44	05.0	0	8.3–9	1,2	300
2	NGC1333-I4A	-	03	29	10.5	31	13	30.5	0	14–18	2,1	350
3	HH211-MM	HH211 *	03	43	56.8	32	00	50.0	0	3.6–5	1,2	300
4	IRAS05173-0555	HH240/1 *	05	19	48.9	-05	52	05.0	0/I	17–26.6	3,4	460
5	HH43-MMS	HH43, HH38, HH64	05	37	57.5	-07	07	00.0	0	3.6–5	3,4	450
6	HH212-MM	HH212 *	05	43	51.5	-01	02	52.0	0	7.7–14	1,2	400
7	HH26IR	HH26 *	05	46	03.9	-00	14	52.0	I	28.8	5	450
8	HH25-MMS	HH25 *	05	46	07.8	-00	13	41.0	0	6–7.2	6,1	450
9	HH24-MMS	HH24 *	05	46	08.3	-00	10	42.0	0	5	7	450
10	IRAS05491+0247 (VLA2)	HH111, HH311, HH113 *	05	51	46.1	02	48	30.6	I	24–42	1,4,8	450
11	NGC2264G-VLA2	- *	06	41	11.0	09	55	59.2	0	12–13	9,1	800
12	IRAS07180-2356	HH72 *	07	20	10.3	-24	02	24.0	I	170	3	1500
13	IRAS08076-3556	HH120	08	09	32.8	-36	05	00.0	I	13–19	3,15	450
14	IRAS08211-4158 (IRS8-2)	HH219 *	08	22	52.1	-42	07	55.0	I	642	10	400
15	#40-3 (IRS17)	- *	08	46	32.6	-43	54	38.9	I	11–245	11	700
16	BHR71-MM (IRS1)	HH321	12	01	44.0	-65	09	00.1	0	7.9–10	2,18	200
17	BHR71 (IRS2)	HH320	12	01	34.0	-65	08	44.0	I	1–3	2,18	200
18	IRAS12515-7641	HH54	12	55	00.2	-76	57	00.0	I	0.22–0.44	16	180
19	VLA1623-243	HH313 *	16	26	26.5	-24	24	31.0	0	1	2	160
20	IRAS18273+0113	HH460	18	29	49.8	01	15	20.8	0/I	45–72	1,12	310
21	R CrA-IRS7	HH99	19	01	55.3	-36	56	21.9	I	3.4	17,19	130
22	L1157-MM	- *	20	39	05.7	68	02	16.0	0	8.4–11	1,2	440
23	IRAS21391+5802	HH593 *	21	40	42.4	58	16	09.7	0	150–350	13,14	750

References: **(1)** Froebrich (2005), **(2)** André et al. (2000), **(3)** Reipurth et al. (1993), **(4)** Molinari et al. (1993), **(5)** Davis et al. (1997), **(6)** Lis et al. (1999), **(7)** Chini et al. (1993), **(8)** Chini et al. (2001), **(9)** Ward-Thompson et al. (1995), **(10)** Caratti o Garatti et al. (2004), **(11)** Giannini et al. (2005a), **(12)** Larsson et al. (2000), **(13)** Beltrán et al. (2002), **(14)** Nisini et al. (2001), **(15)** Persi et al. (1994), **(16)** Cohen & Schwartz (1987), **(17)** Marraco & Rydgren (1981), **(18)** Bourke (2001), **(19)** Wilking et al. (1992)
Note: asterisks in column 3 indicate outlows with a defined morphology, where the knot assignation taken from literature or derived from this work (see Appendix) is certain.

All the raw data were reduced by using IRAF[2] packages applying standard procedures for sky subtraction, dome flat-fielding, bad pixel and cosmic rays removal and imaging mosaic.

Calibration was obtained by means of photometric standard stars observed in both narrow and broad band filters.

Once the narrow band images were calibrated and continuum-subtracted, we detected and measured H$_2$ and [Fe II] fluxes on each knot using the task *polyphot* in IRAF, defining each region within a 2σ contour level above the sky background.

3.2. Spectroscopy

Low resolution spectroscopy was acquired during four different runs at three telescopes, namely ESO-NTT, TNG

[2] IRAF (Image Reduction and Analysis Facility) is distributed by the National Optical Astronomy Observatories, which are operated by AURA, Inc., cooperative agreement with the National Science Foundation.

and AZT-24. As reported in Table 2, we obtained long slit spectra for eight Class 0 jets, with different position angles (P.A.), mostly oriented along each jet axis (except for HH211, where the slit encompasses only the bow-shock in the blue lobe). The spectra of the remaining jets of our sample (with the exception of L1448, where we have no spectra) have been published in our previous papers.

The covered spectral range and resolution are also indicated in Table 2. To perform our spectroscopic measurements, we adopted the usual ABB'A' configuration, for a total integration time between 1200 s and 3600 s per slit. Each observation was flat fielded, sky subtracted and corrected for the curvature derived by long slit spectroscopy, while atmospheric features were removed by dividing each spectrum by a telluric standard star (O spectral type), normalized to the blackbody function at the star's temperature and corrected for hydrogen recombination absorption features intrinsic to the star. The wavelength calibration was retrieved from Xenon and Argon lamps. The flux calibration was obtained from the observation of different

Table 2. Journal of observations - Imaging and Spectroscopy

Object	Telescope/ Instrument	Date of obs. (d,m,y)	Imaging Band	Spectroscopy		
				Wavelength(μm)	$\mathcal{R}$	P.A.($°$)
L1448	TNG / NICS	16/10/2003	[Fe II], H_c			
NGC1333	TNG / NICS	17/10/2003	[Fe II], H_c, H_2, K_c	1.15–2.50	500	34
HH211	TNG / NICS	17/10/2003	[Fe II], H_c, H_2, K_c			
	AZT-24/SWIRCAM	23/10/2004		1.45–2.30	200	90
HH240/1	AZT-24/SWIRCAM	17/11/2004	[Fe II], H			
HH212	ESO-NTT / SofI	11/01/2001	H_2, K'	0.95–2.50	600	22,24
	AZT-24/SWIRCAM	16/11/2004	[Fe II], H			
HH26	AZT-24/SWIRCAM	17/11/2004	[Fe II], H			
HH25	AZT-24/SWIRCAM	17/11/2004	[Fe II], H			
HH24	AZT-24/SWIRCAM	17/11/2004	[Fe II], H			
HH111	ESO-NTT / SofI	11/01/2001	H_2, K'			
NGC2264G	ESO-NTT / SofI	13/03/2003	H_2, K'	0.95–2.50	600	84
	AZT-24/SWIRCAM	17/11/2004	[Fe II], H			
BHR71	ESO-NTT / SofI	02/05/2001	[Fe II], H_2, K'			
	ESO-VLT / ISAAC	15/07/2002	H_2, K'			
HH54	ESO-NTT / SofI	05/06/1999	H_2, K'			
	ESO-VLT / ISAAC	01/01/2005	H_2, K'			
VLA1623–HH313	ESO-NTT / SofI	11/01/2001	H_2, K'	0.95–2.50	600	298,299,305
IRAS18273+0113	ESO-NTT / SofI	05/06/1999	H_2, K'	1.50–2.50	600	328
	ESO-VLT / ISAAC	02/07/2001	[Fe II], H, H_2, K'			
HH99	ESO-NTT / SofI	05/06/1999	H_2, K'			
	ESO-VLT / ISAAC	15/06/2005	H_2, K'			
L1157	TNG / NICS	16/10/2003	[Fe II], H_c	1.15–2.50	500	158,356
IC1396N	TNG / NICS	17/10/2003	[Fe II], H_c, H_2, K_c	1.45–2.50	500	79

Table 3. Camera characteristics

Instrument	FoV ($' \times '$)	pixel scale ($''$/pix)	Ref.
ISAAC	2.5×2.5	0.148	1
SofI	4.9×4.9	0.290	2
NICS	4.2×4.2	0.250	3
SWIRCAM	4×4	1	4

References: **(1)** Cuby et al. (2003), **(2)** Lidman et al. (2000), **(3)** Baffa et al. (2001), **(4)** D'Alessio et al. (2000)

photometric standard stars of the catalogues by Carter & Meadows (1996) and Persson et al. (1998).

The obtained line fluxes were compared with those available in the literature: HH211 (O'Connell et al., 2005), HH212 (Zinnecker et al., 1998; Tedds et al., 2002), HH313 (Eislöffel et al., 2000). The results are consistent with our values considering the calibration errors and the different slit widths.

4. Results & data analysis

4.1. [Fe II] and H_2 imaging

In this section, the results and the analysis obtained from narrow band images are presented. The $1.64\,\mu$m images

were obtained to discover the presence of ionised jets or dissociative regions in bow-shocks associated with known molecular outflows and to compute the [Fe II] radiative contribution to the overall energy budget. The [Fe II] emission regions are always localized in compact spots, representing only a small fraction of the region emitting in H_2. On the new [Fe II] images of the 13 jets presented in this paper (see Table 2), we observe iron emission in 9 objects, namely L1448, HH211, HH240-241, HH212, HH24, HH26, NGC2264G, L1157 and IC1396N. Moreover, considering the entire investigated sample, of 23 outflows, we detect [Fe II] emission in 17 objects (74%), 9 out of 12 from Class 0 (75%), 1 out of 2 from Class 0/I (50%) and 7 out of 9 from Class I YSOs (78%). This indicates that the iron emission is homogeneously distributed over jets of the different YSOs classes and that the presence or not of [Fe II] in the jet is not strictly correlated with the evolutionary stage of the exciting source.

In our analysis of the sample, H_2 images were mainly acquired for photometric purposes. In a few cases, however, the images were also utilized in conjunction with images of the same region taken at different epochs, to derive the proper motion of the knots (see VLA1623, HH54 and HH99 in the Appendix). The kinematical information was particularly useful in those cases where several jets are present in the same region. In such cases it has been possible to disentangle which knots are associated with the source under consideration. The newly discovered knots

(both molecular and ionic), along with their positions and fluxes, are listed in Table 7[3].

In the Appendix, together with a short description, we report the images of those objects not yet published in the literature (mainly [Fe II] emission), or that give some additional information and details on the morphology of the outflows.

4.2. Spectroscopy

In Fig. 1 we show the spectrum of knot A1 in L1157, which can be considered as representative of the whole sample. The most prominent features detected are the H$_2$ lines coming from different upper vibrational levels, ranging from $v = 1$ to $v = 3$. In some cases (HH313 A in VLA1623 and some knots in L1157) we also detect higher vibrational lines ($v = 4$ and 5) coming from energy levels up to 30 000 K.

[Fe II] emission is detected in 20% of the observed knots, that is ∼63% of the objects (5 of 8 spectra reported in Table 2, namely HH211, HH212, VLA1623, IRAS20386, IRAS21391), showing the transitions at 1.644 μm and (often) at 1.257 μm, while the faintest lines (1.534, 1.600, 1.678 μm) are detected just in a few knots (NK1 and SK1 in HH212, HH313 A in VLA1623). Moreover, in HH313 A, we observe (not resolved) the [C I] doublet at 0.983 and 0.985 μm. No other ionic feature is revealed in the analysed spectra, mostly due both to the extinction ($A_\mathrm{v} \geq 5$ mag) and to the low excitation of the observed knots.

In Tables (9-22) we list the fluxes (uncorrected for the extinction) of the identified lines together with their vacuum wavelength. Line fluxes have been obtained by fitting the profile with a single or double Gaussian in case of blending. The uncertainties associated with these data are derived only from the rms of the local baseline multiplied by the linewidths (always comparable with the instrumental profile width). Lines showing fluxes with a S/N ratio between 2 and 3, as well as those blended, have been labelled. Additional uncertainties in the fluxes are derived from the absolute calibration ($\approx 10\%$).

4.2.1. Deriving A_v and H$_2$ temperature

The main quantitative information we can gather from the observed line emission is the reddening towards each knot and the gas temperature characterizing the H$_2$ emission. In the few cases where [Fe II] at 1.53 μm or 1.60 μm has been observed in addition to the 1.64 μm line, the electronic density n_e also can be derived (Giannini et al., 2002).

We have employed all the available H$_2$ ratios to simultaneously evaluate extinction and gas temperature in the framework of ro-vibrational diagrams, where the extinction-corrected column densities, divided by their statistical weights, are plotted against their excitation en-

ergies. If the gas is thermalized, the points in the diagram align in a straight line, whose angular coefficient is the reciprocal of the gas temperature. Line pairs originating from the same level should lie in the same position in the diagram: by varying the A_v value and increasing the goodness of the fit (maximising the correlation coefficient) extinction and temperature can be simultaneously evaluated (see e. g. Nisini et al., 2002b; Davis et al., 2004). To minimize the uncertainties, only the transitions with a S/N>3 and not affected by blending with other lines have been used. If the extinction is relatively low ($A_\mathrm{v} \leq 5$ mag), several bright pairs (e. g. 2-0S(i)/2-0Q(i+2) and 3-1S(i)/3-1Q(i+2) with i=0,1,2...) lying between 1 and 1.35 μm (J band) are observed. In these cases we are able to reduce the uncertainty on A_v to about 1 mag. On the contrary, where the extinction is high (≥ 10 mag), lines in the J band are not visible and the only available pairs involve lines in the range 2.4 -2.5 μm, which are strongly affected by poor atmospheric transmission. In these cases the uncertainty on A_v is 5-10 mag. In Fig. 2, as an example, we show the ro-vibrational diagram of knot A1 in L1157 where the lines coming from different vibrational levels are indicated with different symbols. In this diagram a single temperature LTE gas fits all the lines fairly well. In some cases, however, there is evidence of a stratification in the gas temperature, in which case different temperatures are derived by fitting the various vibrational states. In such cases, a single fit through all the lines gives only a measure of the 'averaged' temperature.

In columns 3 and 4 of Table 4 we report the range of average temperatures and extinctions derived in *each* jet of the sample (see Table 1), while the values for the knots studied in this paper for the first time are given in Table 8. Average temperatures range from 1800 to 4200 K, with typical values around 2500–3000 K, while the extinction spreads from 0 to 15 mag, with the exception of the IRS17 jet where a value of 30 mag is found near the exciting source.

In those cases where the [Fe II] emission is observed, the ratio between the 1.257 and 1.644 μm bright lines has been also used to independently evaluate the extinction. We obtain, for 14 knots of our sample, A_v values that on average are 2.5 mag higher than those derived from the H$_2$ lines. Such result, however, must to be taken with some caution, since the 1.257/1.644 ratio is suspected to systematically overestimate the extinction value (Nisini et al., 2005).

4.3. H$_2$ and [Fe II] luminosities

As a consequence of the high level of emission of H$_2$ and [Fe II] lines in our NIR spectra, we expect that the luminosities of these two species (L_{H_2} and $L_{[\mathrm{Fe\,II}]}$) represent a significant fraction of the overall energy radiated away during the gas cooling (between 10% and 50%, see e. g. Giannini et al., 2001), while most of the remaining energy is emitted at MIR and FIR wavelengths (see e. g. Giannini

---

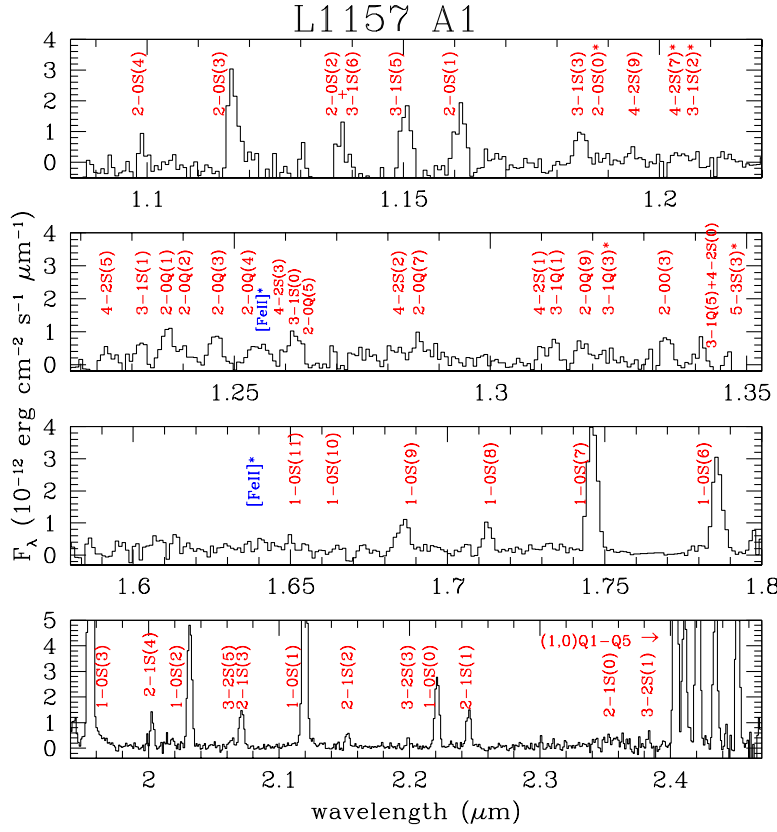[3] Tables 7-22 are only available in electronic form at http://www.edpsciences.org

Fig. 1. 1.1–2.5 μm low resolution spectrum of knot A1 in the L1157 outflow. An asterisk near the line identification marks the detections between 2 and 3 sigma.

et al., 2001; Nisini et al., 2002a). A powerful and commonly used way to estimate L_{H_2} is to directly derive it from the 2.12 μm imaging, by considering $L_{2.12}$ as a fraction of L_{H_2}, whose specific value depends on the gas temperature (in particular $L_{H_2} \sim 0.1 \times L_{H_2}$, if $T \sim 2000$ K). This approximation suffers, however, from two main limitations: i) the lack of knowledge of the extinction, which affects the 2.12 μm luminosity; ii) the presence of different temperature components, as often seen in the rotational diagrams.

The L_{H_2} uncertainty due to the extinction can be quantitatively evaluated by considering that, in our sample, $A_{\rm v}$ ranges typically from 0 to 15 mag (considering also the uncertainties on $A_{\rm v}$, this range is enlarged to 0-25 mag). This implies that, if no extinction is applied, $L_{2.12}$ could be underestimated by up to an order of magnitude. If, however, as in our case, the extinction is measured in spectroscopic observations, the uncertainty on the 2.12 μm intrinsic luminosity is significantly reduced, from 10% to 300%, if the uncertainty on $A_{\rm v}$ is 1 and 10 mag, respectively.

To evaluate the uncertainty on L_{H_2} introduced by the presence of different temperature components, we have plotted in Fig. 3 the 2.12 μm line intensity as a function of the gas temperature in LTE conditions: here it can be no-

ticed how the approximation $L_{2.12} \propto 0.1 \times L_{H2}$ is adequate in a range of temperatures from 1500 to 2500 K. In some of the investigated knots, however, average temperatures higher than 3000 K have been measured (see Table 4), in which cases $L_{2.12}$ represents less than 4% of the total L_{H_2}.

The above considerations have lead us to obtain an accurate measurement of L_{H_2}. We have applied the following procedure: i) we associate each emission knot, traced by narrow band imaging (obtained by us or available in the literature), with the driving YSO, by means of the morphological structure and/or kinematical data (3 objects, see Appendix). Alternatively, when the assignation of a knot remains uncertain, a larger error on L_{H_2} has been applied[4]; ii) the flux of each knot has been evaluated by photometry from the 2.12 narrow band image; iii) once having derived the physical parameters ($A_{\rm v}$, T) of single knots from NIR spectroscopy, we dereddened the 2.12 μm flux, adopting the Rieke & Lebofsky (1985) reddening law, and computed the line ratios with the other H$_2$ lines by applying a simple radiative LTE code. From such ra-

---

[4] As an example, some knots in BHR71, namely HH321 A and knot 6 (see Fig. 3 in Giannini et al., 2004), have been assigned to both sources (IRS 1 & 2) increasing the uncertainty on L_{H_2} by the knot luminosities ($\sim 10^{-2}$ L$_\odot$).
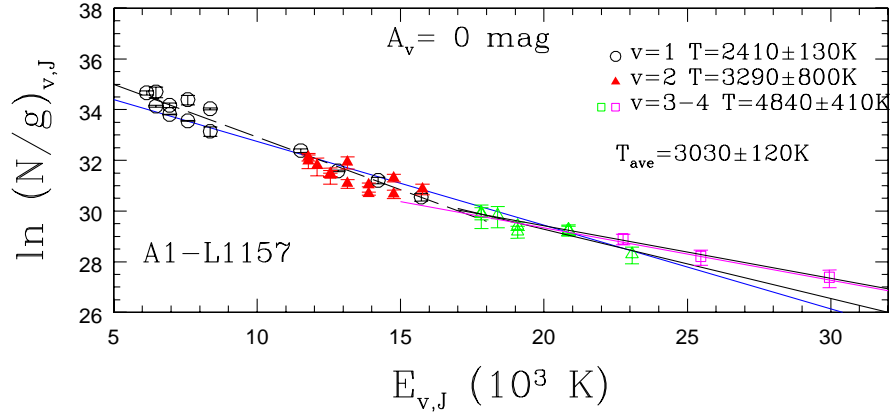
Fig. 2. Rotational diagrams of knot A1 in the L1157 outflow derived from low resolution spectroscopy. Different symbols indicate lines coming from different vibrational levels, as coded in the upper right corner of the box. The straight lines represent the best fit through the v=1, v=2,3,4 (solid line). The derived temperature is also indicated in the upper right corner of the box.
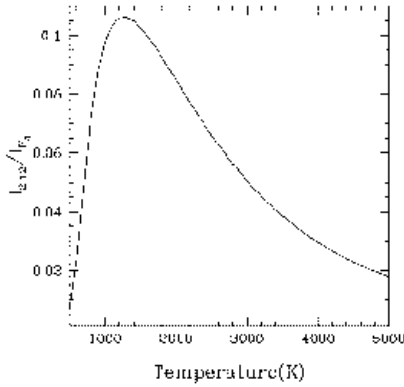

Fig. 3. The plot represents the intensity of the 2.12 μm line with respect to the H$_2$ total intensity as a function of the gas temperature in LTE conditions.

tios, the absolute intensities of individuals lines were computed and added to obtain the total H$_2$ luminosity.

The adopted LTE code computes the line intensities involving levels with $0 \leq v \leq 14$ and $0 \leq J \leq 29$ ($E_{v,J} \leq 50\,000\,K$). Rovibrational energies have been taken from Dabrowski (1984) and the Einstein coefficients from Wolniewicz et al. (1998). We always assume an ortho/para ratio equal to three. To check the validity of our approximation, we compared to the L_{H_2} luminosity computed in LTE at a single temperature with that derived by considering multiple temperature components. An example is given in Fig. 4, which plots the rotational diagram of the knot C in L1157 constructed combining our near-IR data with the $v=0$ mid-IR lines observed by ISOCAM (Cabrit et al., 1999). We can identify three different gas components probed by the $v=0$, $v=1,2$ and $v \geq 3$ transitions and corresponding to the excitation energies $E_{v,J} \leq 6000\,K$, $6000 \leq E_{v,J} \geq 20000\,K$ and $E_{v,J} > 20000\,K$, respectively. The fitted temperature for the 'cold', 'warm' and 'hot' components is 700, 2500 and 5000 K, while, by fitting through only the NIR datapoints, we obtain $T_{avg} = 2600\,K$. The contribution to L_{H_2} coming from each component has been evaluated and compared with that computed if the average temperature is assumed. While the

luminosity of lines with $E_{v,J} > 6000\,\mathrm{K}$ changes of only few percent if the fitted or the average temperature is adopted, the luminosity of the pure rotational lines is slightly underestimated ($\sim$10-15%) if computed by assuming T_{avg}: this can be seen in Fig. 4 by observing that the straight line, which represents the fit through all the NIR data, lies systematically below the points with energy less than $6000\,\mathrm{K}$. However, since this systematic underestimate of L_{H_2} is negligeable with respect to the uncertainties introduced by the A_v determination, we have not corrected our derived LTE values for it.

A complementary way to check how much our L_{H_2} estimate reproduces the real cooling in the considered regions is to compare this value with that obtained by modelling the H$_2$ observed lines with a shock model in which the stratification of the different physical parameters is taken into account. While it is beyond of the scope of this paper to obtain a rigourous modelling for all the observed jets in our sample, we can make this comparison in the few flows we have been salready analyzed through shock models in our previous papers (Giannini et al., 2004; McCoey et al., 2004; Giannini et al., 2005b). We checked that in all these cases our estimated L_{H_2} luminosity is within 15-20% of the luminosity derived from a rigorous shock model fitting and therefore, it represents a good approximation of the H_2 total cooling.

As regards $L_{[\mathrm{Fe\,II}]}$, we have followed the same steps as for the L_{H_2} estimate, by employing a NLTE model to compute the line ratios with respect to the $1.64\,\mu m$ line. The code considers the first 16 fine structure levels of Fe II (see Nisini et al., 2002b, for details). The input parameters are the electron density (n_e) and the gas temperature. The first has been derived for some of the considered knots by (Nisini et al., 2002b), for the others we have assumed a range of $10^3 - 10^5\,\mathrm{cm}^{-3}$, which is typical of the environments where the [Fe II] emission arises. Since all the observed lines have very similar excitation energy ($\sim$ $11\,000$-$12\,000\,\mathrm{K}$) their ratio is not sensitive to the gas temperature; therefore an average value of $10\,000\,\mathrm{K}$ has been assumed for all the emitting regions; we find that $L_{[\mathrm{Fe\,II}]}$ changes by a factor of two in the range of temperatures between $5\,000$–$10\,000\,\mathrm{K}$.

In Table 4 the results of our analysis are reported. For each jet, we give the observed range of H$_2$ temperatures and extinctions (columns 3 and 4), along with the H$_2$ and [Fe II] luminosities (columns 5 and 6). L_{H_2} is, on average, two order of magnitudes greater than $L_{[\mathrm{Fe\,II}]}$, that is, in our sample of jets the cooling occurs mostly through H$_2$ line emission.

5. Discussion

5.1. Comparing the sampled jet properties

Our sample of H$_2$ active jets is comprised of objects belonging to different star forming regions and excited by sources of different ages. This circumstance allows us to investigate whether the physical parameters and chemi-

cal structure of the different jets depend on the evolution of the driving source and/or on the environment. In particular, an evolutionary trend in the jets from a molecular to an ionic composition is expected mainly due to changes in the density of both the jet and the ambient medium where the jet propagates (see e. g. Smith, 2000, 2002). Indeed jets from Class 0 sources travel in the high density gas where most young protostars are embedded. In this framework, non-dissociative C-type shocks that cool mainly through molecular lines, should be favoured . On the other hand, in older protostars (Class I) the jet propagates in a medium at lower density, due to the fact that previous mass loss events have already swept out the ambient gas. In these conditions, dissociative J-type shocks should be favoured due to the lower influence of the local magnetic fields whose strength is a function of the density (see e. g. Hollenbach, 1997). Most of the outflows of our sampled Class 0 are not associated with optical HH, which can be evidence of the scenario described above. However, in the embedded regions surrounding Class 0 sources, optical HHs could be hidden by the extinction, thus remaining undetected. Our images in [Fe II] $1.64\,\mu m$ can be used to signal the presence of embedded dissociative shocks, thus studying if there is a real difference in the characteristics of the shocks between the two classes of sources. Indeed, we detected [Fe II] emission spots in $\sim$74% of the investigated sample, irrespective of the driving source class. Moreover, the NIR spectra in our sample do not exhibit any substantial difference, showing both molecular (H$_2$) and ionic emission ([Fe II], [C I], [S II]) in both Class 0 and Class I flows. Also a more quantitative analysis of the derived jet parameters in Table 4 does not indicate substantial differences between the two groups. Comparing the logarithmic ratio between H$_2$ and [Fe II] outflow luminosities ($log(L_{H2}/L_{FeII})$) in both classes of the sample, we obtain similar values in the younger (2.1$\pm$0.6) with respect the older jets (1.3$\pm$0.7). In addition, if we consider the maximum temperature for both source classes, on average, Class 0 outflows have similar H$_2$ temperatures (3200$\pm$500 K) to Class I outflows (3600$\pm$400 K).

This analysis shows that jet physical properties, as a function of age, cannot be determined when comparing Class 0 outflows with outflows of 'young' Class I sources, as in our case. Differences are more pronounced only when considering sample of sources with a larger spread in age (e. g. Class 0 protostars with 'evolved' Class I and T Tauri stars).

5.2. L_{H_2} and bolometric luminosity

Several works in the past decade have discussed the interplay between the evolutionary properties of young protostars (Class 0/I) and the strength of their associated outflows. Bontemps et al. (1996) were among the first to show that Class 0 protostars drive outflows more powerful than those of Class I sources of the same luminosity, correlating the CO momentum flux (F_{CO}) of a sample
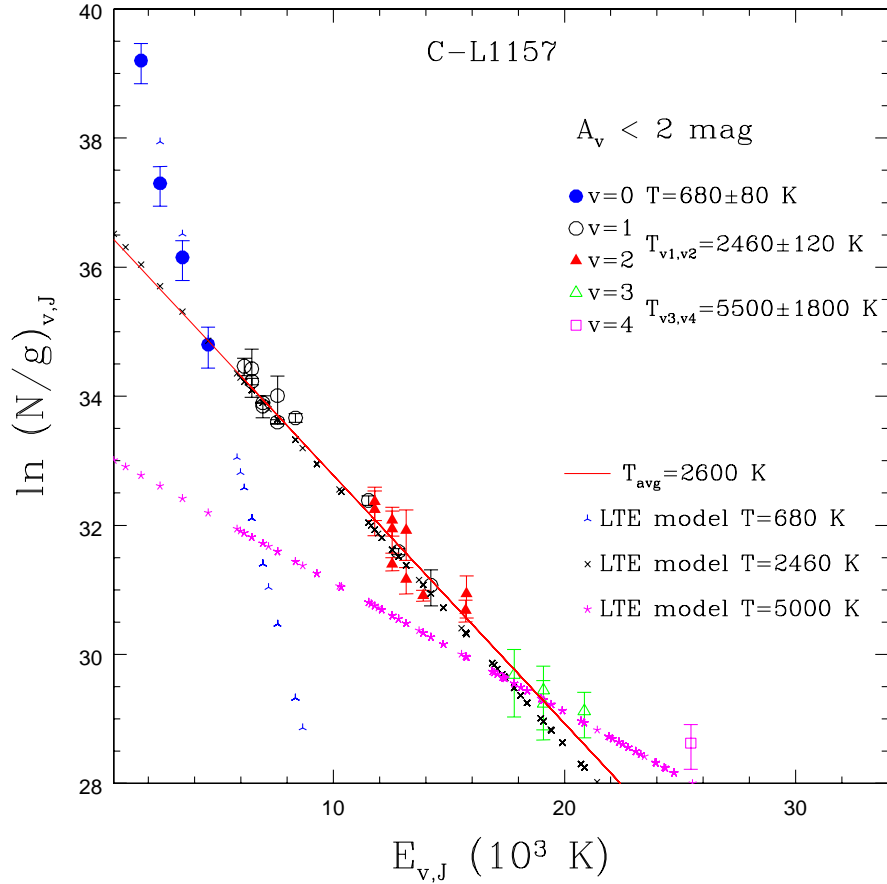
Fig. 4. Rotational diagrams of knot C in L1157. The datapoints from different vibrational levels (including v=0 from Cabrit et al., 1999), are represented with larger symbols and have error bars. LTE H$_2$ models (at T = 680, 2460 and 5000 K) are reported with smaller symbols. The straight line indicates the average temperature adopted (at T = 2600 K).

of embedded protostars with their bolometric luminosity ($L_{\rm bol}$). The larger $F_{CO}/L_{\rm bol}$ efficiency in Class 0 sources has been interpreted as due to the strict relationship between mass accretion and mass loss rates, and to the fact that the fraction of total luminosity due to accretion is larger for Class 0 than the Class I sources. A similar result has been found by Nisini et al. (2002a) using as an indicator of the outflow power the total luminosity radiated in the far IR by OI, H$_2$O and CO, which represent, together with H$_2$, the major coolants in the dense shocks occurring in outflows. In particular, Nisini et al. (2002a) found that $L_{\rm FIR}/L_{\rm bol}$ change from $\sim 10^{-2}$ to $\sim 10^{-3}$ evolving between Class 0 and Class I sources.

Since the H$_2$ emission is more easily observed from the ground than the emission of the other major shock coolants, several works have tried to address if a relationship between L_{H_2} and $L_{\rm bol}$ also exists and depends on the protostellar evolution. Analysing a large sample of H$_2$ jets in Orion A, Stanke (2000) found that only Class I sources roughly follow a correlation between L_{H_2} and $L_{\rm bol}$. Froebrich et al. (2003) present a similar relationship considering a sample composed of mostly Class 0 objects. No clear correlation is found in this sample although a general trend is seen. In these works the L_{H_2} value is al-

ways computed from the observed 2.12 μm flux and correction factor equal for all the flows is applied to take into account the contribution from the other H$_2$ lines and to correct for extinction effects. Here we want to address this issue again, given our more accurate determination of L_{H_2} based on the excitation conditions and $A_{\rm v}$ value for each object. In Fig. 5 we compare the measured outflow H$_2$ luminosity (Table 4) versus the bolometric source luminosity (Table 1), both on a logarithmic scale. Each object has its ID number (as in Table 1). The greater part of the data points lie on a straight line, showing a clear correlation between L_{bol} and L_{H_2}, irrispective of the Class of the exciting source. A few sources, i.e. three Class I and one Class 0/I, are however displaced below this straight line, indicating that their $L_{H_2}/L_{\rm bol}$ ratio is about one order of magnitude lower than in the other sources. The slope follows a law of the type $L_{H_2} \propto L_{bol}^{0.58}$, which closely resembles that found by Shepherd & Churchwell (1996) for the mass loss rates of a sample of outflowing sources (i.e. $\dot{M}_{out} \propto L_{bol}^{0.6}$). However, some caution needs to be exercised in a quantitative interpretation of correlations involving physical quantities both dependent on the distance. An observational bias could be introduced if sources at different distances are considered. Our source sample

Table 4. Parameters of the jets of the sample derived from the H$_2$ and [Fe II] line analysis.

Id	Outflow/HH	Temperature (K)	A_v(H$_2$) (mag)	L_{H_2} (10^{-1} L$_\odot$)	$L_{\text{[Fe II]}}$ (10^{-3} L$_\odot$)
1	L1448	$\cdots$	$\cdots$	1.1±0.4	$1.5^{+0.9}_{-0.7}$
2	NGC1333	2000–2800	5–15	1.0±0.3	not detected
3	HH211	2500–2800	5–10	1.1±0.3	3.1±2
4	L1634 (HH240/1)	2000–4000	2–5	2.4±0.3	39^{+7}_{-4}
5	HH43	4000	1–3	<6	$\cdots$
6	HH212	1700–3000	3–13	1.2±0.4	3.2±0.4
7	HH26	2350–3500	0–3	2.9±0.5	$2^{+1.8}_{-0.5}$
8	HH25	2000–2800	0–8	$1.0^{+0.5}_{-0.2}$	not detected
9	HH24	2200–3500	0–8	$1.4^{+1.6}_{-0.5}$	$2^{+1.8}_{-0.5}$
10	HH111	2200–3500	5–11	$0.5^{+0.2}_{-0.09}$	14.5±7
11	NGC2264G	2100–2800	3–8	$2.8^{+0.6}_{-1.3}$	12±6
12	HH72	2100–3400	5–15	$7.6^{+0.7}_{-0.6}$	8±2
13	HH120	2200–4000	1–5	$2.0^{+1.0}_{-1.1}$	5±1
14	IRS8-2 (HH219)	2000–4200	2–15	0.7±0.1	22^{+6}_{-11}
15	IRS17	1900–3500	5–30	$4.1^{+1.6}_{-0.9}$	12^{+15}_{-7}
16	BHR71 (HH321)	2200–4000	0–2	$1.2^{+0.5}_{-0.8}$	not detected
17	BHR71 (HH320)	2200–3900	0–2	$0.6^{+0.5}_{-0.4}$	not detected
18	HH54	2500–3300	1–3	0.18±0.03	1.6±0.5
19	VLA1623-243 (HH313)	2000–3100	4–15	$0.40^{+0.06}_{-0.14}$	0.5±0.2
20	IRAS18273+0113	2200–2600	5–10	0.4±0.2	not detected
21	HH99	2000–3600	4	0.07±0.04	6±2
22	L1157	2100–3100	0–2	1.7±0.1	0.7±0.2
23	IC1396N	2400–2700	5–15	$6.1^{+3.8}_{-1.6}$	20^{+18}_{-7}

Note: the ranges (min-max) of T and A_v observed in the outflow knots are reported.

spans distances ranging from 130 pc to 1.5 kpc and a correlation, although with a large scatter (linear regression gives a correlation coefficient r=0.65) is seen in a Log(D(pc)) vs Log(L_{bol}) plot (see Fig. 6). Given the small scatter in the correlation derived in Fig. 5 (the linear regresion gives a correlation coefficient r=0.99) we can conclude that there is a dependence of L_{H_2} on L_{bol}, whose exact form we cannot deduce from the data.

To test the accuracy of our analysis, we report in Fig. 7 the same Log(L_{bol}) vs Log(L$_{H_2}$) plot but for the subsample of objects showing a bipolar structure or a clear morphology (see Sect. 2). We find for them the same correlation obtained in the complete sample.

While Class 0 sources all show the same L_{H_2}/L_{bol} efficiency, the Class I sources of our sample have a less defined behaviour, and a clear separation between the two class of sources is not seen, at variance with the results found by Nisini et al. (2002a), adopting the far IR line cooling as a tracer of the outflow power.

Such a different behaviour between L_{H_2} and L_{FIR} could be due to the way in which the shock luminosity is distributed among the various cooling channels, depending on the local physical conditions. In particular, the different critical densities of NIR H$_2$ lines ($\sim 10^3 - 10^4$ cm^{-3} at $T = 2000$ K) and FIR CO and H$_2$O lines ($10^5 - 10^9$ cm^{-3}) may play a role. In high density environments the H$_2$ line intensity per unit volume has already reached its maxi-

mum LTE value and the cooling by other species (CO and H$_2$O in particular) becomes the dominant contribution.

In order to verify this hypothesis we have compared L_{H_2} to L_{FIR} derived in previous works (Giannini et al., 2001; Nisini et al., 2002a) for the 9 objects of our sample where this value is available. Although only two Class I objects are in this restricted sample, we observe a lower ratio (L_{H2}/L_{FIR}) in Class 0 objects (0.9±0.7) with respect to Class I ($\sim$13), suggesting that the density could play a major role in determining the cooling channels.

The plot in Fig. 5 also shows that among our sample of Class I objects there is a significant number of objects ($\sim$17%) having an L_{H_2}/L_{bol} ratio about an order of magnitude lower than the other sources. We have checked that for these sources systematic errors in the derivation of L_{H_2}, due e. g. to a missing contribution from not considered emission knots or due to a wrong assignment of the exciting source, are not significant. In a few cases, it is not possible to completely exclude the occurence of parsec-scale outflows, which, in principle, could introduce a bias in the results. For example, HH111 is part of a giant outflow (composed of HH113, HH311 and probably HH182 Reipurth et al. , 1997; Wang et al. , 2005) and there are no NIR data available in the literature for the remaining outflow componets. However, even assuming that each of the other outflow components contribute as much as HH111, the total H$_2$ luminosity would be about three times higher than the presently estimated value. Such an effect will
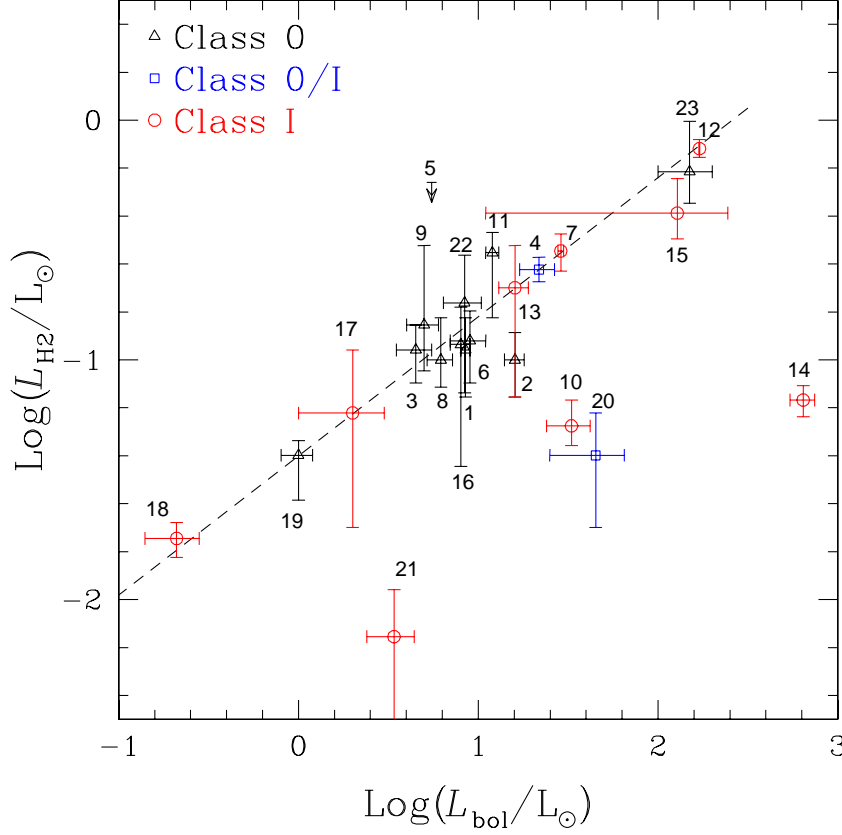
Fig. 5. Measured outflow H_2 luminosity (reported in Table 4) versus the bolometric source luminosity (listed in Table 1). Each object has its ID number. Outflows from Class 0 are marked with a circle, Class I with triangles and Class 0/I with squares. The dashed line represents the derived best-fit: $log(L_{H_2}/L_{\odot}) = (0.58 \pm 0.06)log(L_{bol}/L_{\odot}) - (1.4 \pm 0.04)$, computed without considering the four data points (ID 10, 14, 20 and 21) which fall definitively outside the relationship.

not appreciably change the location of this object in the $Log(L_{bol})$ vs $Log(L_{H_2})$ plot. It is more likely that the Class I sources with the lower L_{H_2}/L_{bol} are more evolved objects, where L_{bol} is no longer dominated by the accretion luminosity and the mass loss rate is declining. This result partially reflects the broader properties in terms of evolution among the Class I objects, where sources with different accretion properties are found (see e. g. Nisini et al., 2005).

Most of the sources of our sample have been mapped in CO and an estimate of the mechanical power ($L_{mech} = \frac{1}{2}\dot{M}_{out}v_{CO}^2$) in the molecular outflow is available in the literature. Assuming momentum balance in the shocked region between the stellar jet and the ambient medium, we expect that the outflow mechanical power should be roughly equal to the total power radiated by the shock L_{rad} (Davis & Eislöffel, 1995).

For those sources of our sample observed also in the far IR, we can provide a quantitative estimate of the total shock radiated luminosity by adding the L_{H_2} and the L_{FIR} due to the other major coolant. We find a mean ratio L_{rad}/L_{mech} around unity (1.1±0.6), which indicates

that the considered shocks may have enough power to accelerate the whole molecular ouflow.

6. Conclusions

We have measured the cooling and the physical properties at NIR wavelengths of a sample of protostellar jets (23 objects), originated by Class 0 and I low-intermediate solar mass YSOs, presenting new spectroscopic and imaging observations of 15 objects. We have investigated how the derived properties are correlated with the evolution of the jets and their exciting sources. The main results of this work can be summarized as follows:

- [Fe II] emission in active H_2 jets has been systematically investigated to define the occurrence of embedded ionized gas in young outflows. [Fe II] emission spots are observed in ∼74% of the investigated sample, irrespective of the driving source class. This indicates that dissociative-shocks are common even in high-density embedded regions which do not show optical HH objects.
- H_2 line ratios have been used to estimate the visual extinction (A_v) and average temperature of the molec-
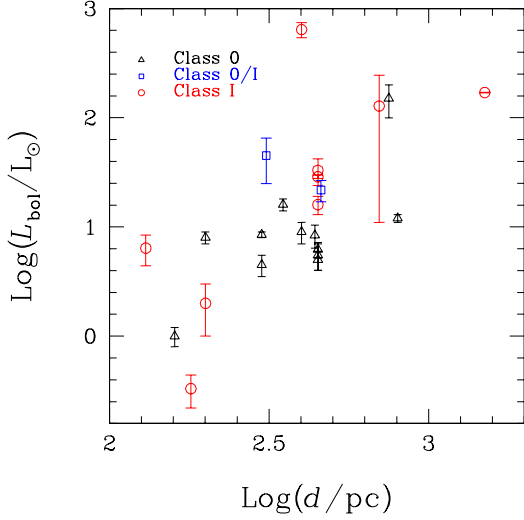
Fig. 6. Bolometric luminosity (L_{bol}) of the 23 sources of our sample, plotted as a function of the source distance from the Sun. Class 0 sources are marked with a circle, Class I with triangles and Class 0/I with squares.
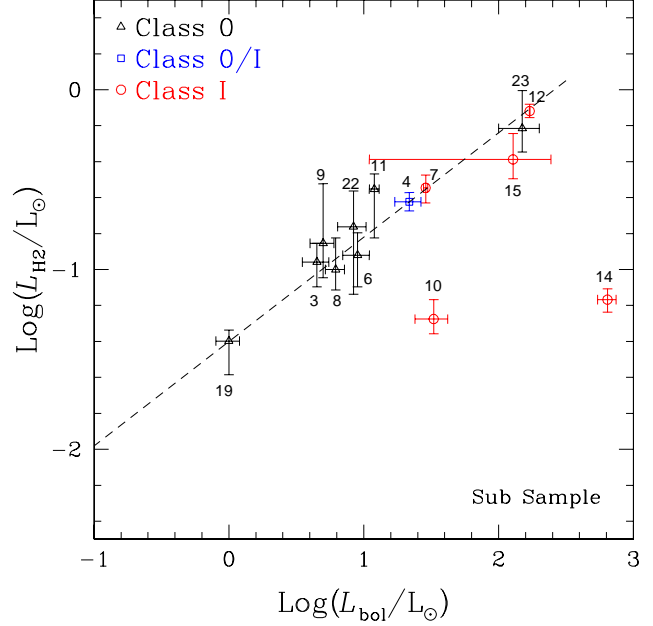

Fig. 7. Measured outflow H$_2$ luminosity (reported in Table 4) versus the bolometric source luminosity (listed in Table 1) for a sub-sample of objects, showing a clear morphology (see Table 1, col. 3). Labels are as in Fig. 5. The dashed line is the best-fit derived from the entire sample and reported in Fig 5.

ular gas. When observed, the [Fe II] $1.53/1.64\,\mu$m ratio was used to determine the electron density (n_e) of the atomic gas component. A_v values range from $\sim$2 to $\sim$15 without any evidence of higher extinction associated with the Class 0 flows. The H$_2$ average gas temperatures range between $\sim$2000 and 4000 K. In several knots, however, a stratification of temperatures is found with maximum values up to 5000 K. Generally, gas components at different temperatures are associated with the knots also showing [Fe II] emission while thermalized gas at a single temperature is most commonly found in knots emitting only in molecular lines.

- We have computed the total cooling due to H$_2$ and [Fe II] (L_{H_2}, L_{FeII}) adopting the parameters derived from the line ratio analysis in the single knots and the H$_2$ 2.12 μm, [Fe II] 1.64 μm luminosities derived from the narrow band imaging. The determination of L_{H_2} strongly depends on the local gas conditions and in particular on the A_v value, therefore the often-used approximation $L_{2.12} \sim 0.1 \times L_{H_2}$ can be wrong by up to an order of magnitude if a proper reddening is not applied.

- By comparing the measured outflow H$_2$ luminosity with the source bolometric luminosity (assumed representative of the accretion luminosity), we find that for $\sim$83% of the sources there is a correlation between these two quantities, with $L_{H_2}/L_{bol}$$\sim$0.04. A small sample of four sources, however, display an efficiency L_{H_2}/L_{bol} lower by about an order of magnitude. We interpret this behaviour in terms of evolution, with the

sources which are less efficient H$_2$ emitters are more evolved than the others.

- We also find that there is not a clear separation in terms of L_{H_2}/L_{bol} efficiency between Class 0 and Class I sources (although the four objects with the lower L_{H_2}/L_{bol} value are all from Class I or intermediate Class 0/I). This partially reflects the large heterogeneity between the evolutionary properties among Class I, which include sources with very different accretion properties. In addition, the efficiency of the H$_2$ cooling in a dense ambient medium, likely characterizing the Class 0 environment, can be limited by the relatively small critical density of H$_2$ IR lines ($\sim$10^3-10^4 cm^{-3}). Indeed, the total cooling of flows from Class 0 sources prevalently occurs at far IR wavelengths through CO and H$_2$O emission lines and thus can be underestimated considering only the H$_2$ contribution.

- On the basis of the observational experience, accumulated over the last decade, it maybe empirically adequate to refine the concept of Class I objects. According to the present analysis of the H$_2$ jets, we suggest to define a new Class 0.5, which is composed (as a starting point) of objects defined as Class I YSOs (according to Lada & Wilking, 1984), but presenting a L_{H_2}/L_{bol} ratio similar to that of Class 0 sources (i.e. $\sim$0.04 or higher). We would classify as Class 0.5 the following objects: $IRAS\,05173 - 0555$, HH26IR, $IRAS\,07180 - 2356$, $IRAS\,08076 - 3556$, #40-3 (IRS17), BHR71(IRS2), $IRAS\,12515 - 7641$.

Obviously, this tentative classification should be confirmed with further observations.

References

André, P., Martin-Pintado, J., Despois, D., Montmerle, T. 1990, A&A, 236, 180

André, P., Ward-Thompson, D., Barsony, M. 2000, in Protostars and Planets IV, 59, University of Arizona Press; eds. Mannings, V., Boss, A.P., Russell, S.S.

Baffa, C., Comoretto, G., Gennari, S., et al. 2001, A&A, 378, 722

Bally, J., Devine, D. & Reipurth, B. 1996, ApJ, 473, L49

Barsony, M., Ward-Thompson, D., André, P., 0'Linger, J. 1998, ApJ, 509, 733

Beltrán, M.T., Girart, J.M., Estalella, R. 2002, ApJ, 573, 246

Bontemps, S., André, P., Tereby, S., Cabrit, S. 1996, A&A, 311, 858

Bontemps, S., André, P., Kaas, A. A.et al. 2001, A&A, 372, 173

Bourke, T.L. 2001, ApJ, 554, 91

Cabrit, S. & Bontemps, C. 1992, A&A, 261, 274

Cabrit, S., Bontemps, S., Lagage P.O., Sauvage, M. et al. 1999, in The Universe as Seen by ISO, p.449: eds. P. Cox & M. F. Kessler.

Caratti o Garatti, A., Giannini, T., Lorenzetti, D., et al. 2004, A&A, 422, 141

Carter, B.S., Meadows, V.S. 1995, MNRAS, 276, 1052

Cohen, M., Schwartz, R.D. 1987, ApJ, 316, 311

Choi, M. 2001, ApJ, 553, 219

Chini, R., Krugel, E., Haslam, C.G T., et al. 1993, A&A, 272, L5

Chini, R., Ward-Thompson, D., Kirk, J.M., et al. 2001, A&A, 369, 155

Codella, C., Bachiller, R., Nisini, B., et al. 2001, A&A, 376, 271

Cuby, J-G., Lidman, C., Johnson, R., Moutou, C. 2003, ISAAC User Manual

D'Alessio, F., et al. 2000, Proc. of the SPIE Symp. on Astronomical Telescopes and Instrumentation; eds. M. Iye, & A. F. M. Moorwood, 4008, 748

Dabroski, I. 1984, Can. J. Phys., 62, 1634

Davis, C.J. & Eislöffel, J. 1995, A&A, 300, 851

Davis, C.J. & Smith, M.D. 1995, ApJ, 443, L41

Davis, C.J., Ray, T.P., Eislöffel, J., Corcoran, D. 1997, A&A, 324, 263

Davis, C.J., Smith, M.D., Eislöffel, J., Davies J.K. 1999, MNRAS, 308, 539

Davis, C.J., Matthews, H.E., Ray, T.P., Dent, W.R.F., Richer, J.S. 1999, MNRAS, 309, 141

Davis, C.J., Varricatt, W.P., Todd, S.P., Ramasy Howat, S.K. 2004, A&A, 425, 981

Eiroa, C., Palacios, J., Eislöffel, J. et al. 1997, in IAU Symposium 182, 103; eds. F. Malbet & A. Castets

Eislöffel, J. 2000, A&A, 354, 236

Eislöffel, J., Smith, M. D., Davis, C. J. 2000, A&A, 359, 1147

Eislöffel, J., Froebrich, D., Stanke, T., McCaughrean, M.J. 2003, ApJ, 595, 259

Fich, M. & Lada, C.J. 1997, ApJ 484, L63

Froebrich, D., Smith, M.D., Hodapp, K.W., Eislöffel, J. 2003, MNRAS, 346, 163

Froebrich, D. 2005, ApJS 156, 169

Giannini, T., Nisini, B., Lorenzetti, D. 2001, ApJ, 555, 40

Giannini, T., Nisini, B., Caratti o Garatti, A., Lorenzetti, D. 2002, ApJ, 570, L33

Giannini T., McCoey, C., Caratti o Garatti, A. et al. 2004, A&A, 419, 999

Giannini, T., Massi, F., Podio, L. et al. 2005, A&A, 433, 941

Giannini, T. et. al. 2005b, in prep.

Gibbs, M. & Davis, C.J. 1998, MNRAS, 298, 644

Gomez, M., Stark, D.P., Whitney, B.A., Churchwell, E. 2003, AJ, 126, 863

Hamaguchi, K., Corcoran, M.F., Petre, R. et al. 2005, ApJ, 623, 291

Hartigan, P., Raymond, J., Hartmann, L. 1987, ApJ, 316, 323

Harvey, P.M., Wilking, B.A. & Joy, M. 1984, ApJ, 278, 156

Hodapp, K.-W. & Ladd, E.F. 1995, ApJ, 453, 715

Hollenbach, D. 1997, in IAU Symposium N 182, p. 181; eds. B. Reipurth & C. Bertout.

Hughes, J. & Hartigan, P. 1992, AJ, 104, 680

Herbst, T.M., Beckwith, S.V.W. & Robberto, M. 1997, ApJ, 486, 59

Khanzadyan, T., Gredel, R., Smith, M.D., Stanke, T. 2004, A&A, 426, 171

Knee, L.B.G. 1992, A&A, 259, 283

Lada, C.J. & Wilking, B.A. 1984, ApJ, 287, 610

Larsson, B., Liseau, R., Men'shchikov, A.B. et al. 2000, A&A, 363, 253

Lidman, C., Cuby, J-G., Vanzi, L. 2000 SofI User Manual, ESO

Liseau, R., Sandell, G. & Knee, L.B.G. 1988, A&A, 192, 153

Lis, D.C., Menten, K.M., Zylka, R. 1999, ApJ, 527, 856

Looney, L.W., Mundy, L.G., Welch, W. J. 2000, ApJ, 529, 477

Lorenzetti, D., Giannini, Vitali, F. et al. 2002, ApJ, 564, 839

Margulis, M., Lada, C.J., Snell, R.L. 1988, ApJ, 233, 316

Marraco, H.G. & Rydgren, A.E. 1981, AJ, 86, 62

McCaughrean, M.J., Rayner, J.T. & Zinnecker, H. 1993, ApJ, 436, L189

McCoey, C., Giannini, T., Flower, D.R., Caratti o Garatti, A. 2004, MNRAS, 353, 813

Molinari, S., Liseau, R., Lorenzetti, D. 1993, A&AS, 101, 58

Mundt, R., Ray, T. P., Raga, A. C. 1991, A&A, 252, 740

Nisini, B., Massi, F., Vitali, F., et al. 2001, A&A, 376, 553

Nisini, B., Giannini, T., Lorenzetti, D. 2002a, ApJ, 574, 246

Nisini, B., Caratti o Garatti, A., Giannini, T., Lorenzetti, D. 2002b, A&A, 393, 1035

Nisini, B., Bacciotti, F., Giannini, et al. 2005, A&A in press

Nutter, D.J., Ward-Thompson, D., André, P. 2005, MNRAS, 357, 975

O'Connell, B., 2005, PhD thesis, Trinity College Dublin

O'Connell, B., Smith, M.D., Froebrich, D. et al. 2005, A&A, 431, 223

Persi, P., Ferrari-Toniolo, M., Marenzi, A.R.et al. 1994, A&A, 282, 233

Persson , S.E., Murphy, D.C., Krzeminski, W. al. 1998, AJ, 116, 2475

Porras , A., Allen, L.E., Muzerolle, J. et al. 2004, AAS meeting, 205, #174.10

Reipurth, B., Chini, R., Krugel, E., Kreysa, E., Sievers, A. 1993, A&A, 273, 221

Reipurth, B., Bally, J. & Devine, D. 1997, AJ, 114, 2708

Reipurth, B., Armond, T., Raga, A., Bally, J. 2003, AJ, 593, L47

Rieke, G.H., Lebofsky, M.J. 1985, ApJ, 288, 618

Saraceno, P., André, P., Ceccarelli, C., Griffin, M., Molinari S. 1996, A&A, 309, 827

Shepherd, D. & Churchwell, E. 1996, ApJ., 472, 225

Smith, M.D., 2000, Irish Astron.J., 27, 25

Smith, M.D., 2002, in The Origins of Stars and PLanets; the VLT View, ESO Astrophysics Symposia; eds. J. Alves & M. McCaughrean

Solf, J. 1987, A&A, 184, 322

Stanke, T. 2000, PhD thesis, Univ. of Postdam

Tedds, J.A., Smith, M.D., Fernandes, A.J.L., Davis, C.J. 2002, RMxAA, 13, 103

Wang, H., Mundt, R., Henning, T., Apai, D. 2004, ApJ, 617, 1191

Wang, H., Stecklum, B. & Henning, Th. 2005, A&A, 437, 169

Ward-Thompson, D., Eiroa, C., Casali, M.M. 1995, MNRAS, 344, 809

Wilking, B.A, Greene, T.P, Lada, C.J. et al. 1992, ApJ, 397, 520

Wilking, B.A, McCaughrean, M.J., Burton, M. et al. 1997, AJ, 114, 2029

Wolniewicz, L., Simbiotin, J., Dalgarno, A. 1998, ApJS, 115, 293

Ziener, R. & Eislöffel, J. 1999, A&A, 347, 565

Zinnecker, H., McCaughrean, M.J., Rayner, J.T. 1998, Nature, 394, 862
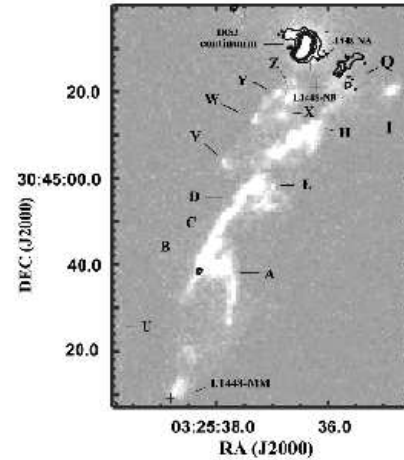
Fig. 8. L1448 outflow blue lobe: H$_2$ ($2.122\,\mu m$) image (particular from Davis & Smith, 1995) with the [Fe II] (continuum-subtracted) contours. On the IRS3 source the continuum emission from the nebula is still present as a residual.

7. Appendix

Here we give a short description of each newly analysed region and comments on the new data (NIR imaging and spectrscopy) presented in this paper.

7.1. L1448

L1448 is in the Perseus dark cloud, containing several YSOs, that drive powerful outflows (see e. g Davis & Smith, 1995; Eislöffel, 2000). Among them, the Class 0 L1448-MM (or C) drives an extremely high velocity outflow. The blueshifted lobe (north-west of L1448-MM) (Fig. 8) is composed of (at least) three distinct curved jets (Eislöffel, 2000), roughly parallel, originating the millimetric source itself (the main jet) and two other embedded sources (L1448 NA, knots Z,Y,X,W,V and NB, knot Q Barsony et al., 1998).

In this blue lobe we detected [Fe II] emission (see contours in Fig. 8). Surprisingly, in the main jet knot A is not positioned at the apex of the bow-shock, but in a region located between the west wing and knot B.

A jet-like structure, spatially coincident with knot Q, is clearly visible about 10″ SW of the IRS3 nebula and likely originates L1448 NB. A second emission, a few arcsecs south of the jet, is observed. This could be a residual of a diffuse nebulosity (also observed by Davis & Smith, 1995) or a real [Fe II] emission from the main jet.

7.2. NGC1333-I4A outflow

NGC 1333 is a reflection nebula associated with a region of recent star formation in the Perseus molecular cloud, with several Class 0 and I sources. Among them the IRAS

4A binary system (Class 0) drives a well collimated bipolar outflow with several H$_2$ knots (Liseau et al., 1988; Hodapp & Ladd, 1995; Choi, 2001). The blue lobe (NE direction) is made up of the H$_2$ knots ASR 57, HL 10, 11 and, possibly, HH347 (Bally et al., 1996), and the red lobe of HL 6, 5 and 3.

Our NIR spectroscopy indicates an high visual extinction (10-15 mag) in these knots, increasing towards the source. The high extinction explains why we do not detect some of the knots identified at mid-IR wavelengths by Spitzer (Porras et al., 2004).

7.3. HH211

HH211, discovered by McCaughrean et al. (1993) in the Perseus dark cloud, is one of the smaller known outflows ($\sim$0.16 pc). Eislöffel et al. (2003), with a deep H$_2$ image, observed a highly collimated jet (knot G) and counter-jet structure within an excavated rim-brighted cavity, showing a strong continuum emission. Combined with this continuum, O'Connell et al. (2005) detected [Fe II] emission, indicating the presence of dissociative shocks inside the outflow. In our continuum-subtracted [Fe II] image, the ionic emission on the blue lobe (SE) clearly comes from the axis of the bow-shock (knot I), while on the red lobe side, it is located at the end of the counter-jet (knot F) and the external bow-shocks (knots D and C). The knot positions along with the fluxes are reported in Table 7. As expected, the measured flux values are lower than in O'Connell et al. (2005), because the continuum has been removed.

7.4. HH240/1

The spectacular HH240/1 objects are located inside L1634 in Orion and include four pairs of symmetrical H$_2$ knots, mostly bow-shocks, originating in the intermediate Class 0/I YSO $IRAS05173-0555$ (Davis et al., 1997; Froebrich, 2005). Our H$_2$ imaging and NIR spectroscopy has been presented in a previous paper (Nisini et al., 2002b). New [Fe II] images of the outflow reveal strong compact emission from the inner bow-shocks HH240 A (F$_{1.64\mu m}$ $\sim 9 \times 10^{-14} erg \ s^{-1} \ cm^{-2}$) and HH241 A (F$_{1.64\mu m} \sim 10^{-14} erg \ s^{-1} \ cm^{-2}$), roughly located at the apex of the bows. Unfortunately, the morphology of the iron emitting regions are poor resolved, due to the relatively low spatial resolution of the camera (1$''$/pixel). No other [Fe II] emission is observed along the flow.

7.5. HH212

Discovered by Zinnecker et al. (1998), HH212 is located in the Orion B giant molecular cloud. Together with HH211, it represents an H$_2$ jet prototype, visible only in the IR, with the exception of the most distant bow-shocks, which also appears in [S II] emission CCD images. The H$_2$ knots, centered around the source HH212–MM or

$IRAS05413-0104$, are highly symmetric and mark the periodical outflow ejection mass. In our [Fe II] (continuum-subtracted) image, the knots NK1 and SK1 (nearby the source) show a strong iron component, revealed in our NIR spectra as well. A much fainter emission is visible towards the external knots and bow-shocks NK7, NB1 and SB1 (see Table 7).

No other ionic component has been detected in the NIR spectra (0.95–2.5 μm) of these knots (see Table 11), likely due to the high visual extinction (10–15 mag) of the inner part of the jet.

7.6. HH24-26 region

This region is placed in the L1630 Orion dark cloud and exhibits a very complex morphology due to the high star formation activity. Three YSOs of this region are included in our sample, namely HH24–MM, HH25–MM and HH26IRS. HH24–MM (Chini et al., 1993) is a Class 0 YSO, driving a highly collimated jet (Bontemps et al., 1996) (Fig. 9) (indicated as knot L, following Eislöffel et al., 2000). In the north-western direction, roughly along the jet axis, there is the bright knot HH24 A, but it is not clear if it is part of the same outflow or not (see e.g. Solf, 1987; Eislöffel et al., 2000). The [Fe II] (continuum-subtracted) contours in Fig. 9 distinctly outline a jet escaping from the YSO SSV 63E (observed through [S II] as well) (see e.g. Mundt et al., 1991; Eislöffel et al., 2000), coincident with knots C, E and, partially, with HH24 A. Here the brightest iron feature matches the H$_2$ structure labelled 1 in Fig. 9 (lower left corner). On the contrary, knot 3 has a well defined bow-shock shape pointing backwards to HH24–MM. Knot 2 is well aligned and could be part of the outflow too. Thus HH24 A is probably composed of two overlaying jets, coming from the two sources.

Knots D, G and N (see Fig. 9, main picture) trace another outflow, which seems to be emanated from SSV63E as well. In this case the YSO would be a doublet, even if we do not resolve the components in our image. Vice versa, two distinct sources compose SSV 63W, separated by about 2$''$. The northern star can be associated with knots J and K, while the southern with knot B.

[Fe II] imaging of the HH26 region shows a strong emission ($F_{1.64\mu m} \sim 10^{-14} \, \mathrm{erg \, s^{-1} \, cm^{-2}}$) from knot A, whereas no iron emission is detected from HH25.

7.7. NGC2264G

The high velocity outflow NGC2264G in the Mon OB1 molecular cloud (at a distance of 800 pc) has been mapped in CO J=1-0 and 2-1 by several authors (e.g. Margulis et al., 1988; Fich & Lada, 1997), showing a peculiar symmetrical deflected pattern, probably due to an abrupt change in the rotational axis. In our image (Fig. 10), the H$_2$ emission is more extended than in previous images (Davis & Eislöffel, 1995), matching very well the CO contours (from Fich & Lada (1997)) and appearing as a parsec scale flow
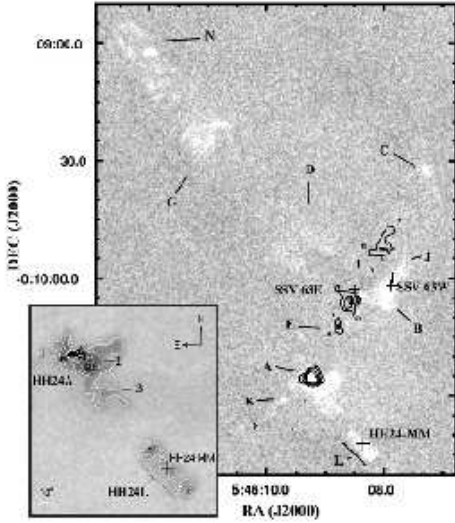
Fig. 9. HH24 region: H_2 ($2.122\,\mu m$) image (continuum-subtracted) with 3, 4, 5, 6σ [Fe II] (continuum-subtracted) contours.

(about 1.6 pc). The H_2 emission in the blue lobe (western direction) could be even wider than observed, since another CO clump has been detected just outside the image. On the [Fe II] (continuum-subtracted) image, not reported here, we also detect a 3σ emission (with flux $F_{1.64\mu m} = 1.3\pm0.4\,\mathrm{erg\,s^{-1}\,cm^{-2}}$) about $5''$ west of knot A1 and coincident with the peak of the CO outflow. The new groups of detected knots (G, H and I), labelled following Davis & Eislöffel (1995), with their fluxes and positions are reported in Table 7 and are shown in detail in Fig. 11.

NIR spectra of the blue lobe show only low excitation H_2 emission ($v \leq 3$) (see Table 13).

7.8. VLA1623

Located in the ρ Ophiuchi cloud (d$\sim$160 pc), the VLA1623 molecular outflow (André et al., 1990) shows a very complex structure, probably because VLA1623 is a binary system (Looney et al., 2000). H_2 emission was first detected by Davis & Eislöffel (1995) and a detailed classification can be found in Gomez et al. (2003).

In Fig. 12 we present our H_2 continuum-subtracted image of the region that clearly exhibits two outflows with the typical "S-shape" originating in the rotational axis precession of the exciting sources. The newly detected knots (GSWC2003–17b, 14h and 14i) (see Fig. 12, upper left corner) are labelled following the Gomez et al. (2003) classification and their positions and fluxes are reported in Table 7.

To better define which knots arise from the VLA1623 system, we computed the proper motions (PMs) and po-

Table 5. Tangential velocities ($\mathrm{km\,s^{-1}}$) and position angles ($^\circ$) of the studied knots in VLA1623.

knot	v_{tan} ($\mathrm{km\,s^{-1}}$)	P.A. ($^\circ$)
HH313 A	60±15	315±12
HH313–A2	46±15	333±24
HH313 B	46±16	243±14
GSWC2003–13a	46±16	297±14
GSWC2003–13b	58±15	315±12
GSWC2003–14e	86±15	315±12
GSWC2003–17b	74±15	303±12

sition angles (P.A.) (Table 5) for the north-western part of the outflows (see Fig. 12, upper left corner), comparing our H_2 image (March 2003) with that published by Davis & Eislöffel (1995) (April 1993) (see Caratti o Garatti et al., 2004, for the details on the adopted technique).

As suggested by Eislöffel et al. (2000), we find that HH313 B is not generated by the VLA 1623 source. Its position angle, derived from the proper motion measurement ($46\pm16\,\mathrm{km\,s^{-1}}$), is roughly 243° (counterclockwise), hence the source could be inside the nebula that hides the source GSS30 or it could be part of a larger flow that includes the objects HH79 and HH711 located outside our image (M.D. Smith priv. comm.).

HH313 A is composed of two different structures (Fig. 12 lower left corner). The bow-shock (knots A1, A3 and A4 Davis et al., 1999) is generated by VLA1623, showing a P.A. of $304^\circ\pm8^\circ$ and a proper motion of $60\pm15\,\mathrm{km\,s^{-1}}$, that, corrected by its inclination angle with respect to the plane of the sky ($\sim15^\circ$), is in good agreement with model predictions (Davis et al., 1999). The second component (knot A2) has a slower motion ($46\pm15\,\mathrm{km\,s^{-1}}$) with a P.A. of $333^\circ\pm24^\circ$. From the PM analysis it is not clear if it is correlated with the bow-shock or not.

The remaining knots analysed clearly originate in the VLA system and their slightly different P.A. follow the precession of the two outflows.

In the large field image (Fig. 12) we also detect two new ouflows not originating in VLA1623. The first is composed of knots A and B, southward of HH313, symmetrically situated with respect to ISO–OPH26, a Class II YSO (Bontemps et al., 2001). The second outflow lies southward of VLA1623 and is traced by two bow-shocks (labelled C and D), possibly generated by $IRAS16223 --2421$, located outside our image. The two bow-shocks were also identified by Khanzadyan et al. (2004) (knots i and h in their field 10-01) as part of a larger outflow made up of several knots roughly aligned with YLW 31, a Class II protostar, lying near the position of the IRAS source.

Outflow NIR spectra (Table 14-17) reveal only ionic emission in HH313 A ([Fe II] and [C I]), whereas in the remaining knots only low excitation H_2 emission lines ($v \leq 3$) are detected.
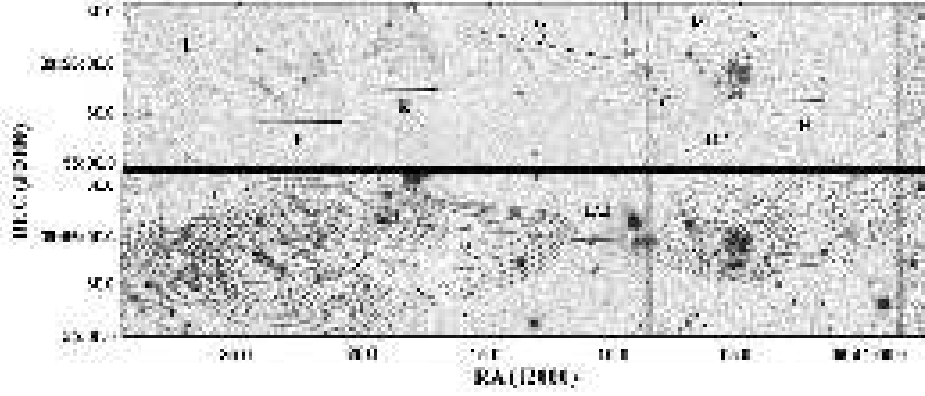
Fig. 10. NGC2264G outflow: H$_2$ (2.122 μm) image + (continuum-subtracted). CO contours from Fich & Lada (1997).

7.9. HH54

HH54 is situated in a low mass star-forming region of the Chamaleon dark clouds at a distance of about 200 pc (Hughes & Hartigan, 1992). There are at last two driving sources candidates for the outflow, IRAS 12522-7640 and IRAS 12515-7641 (Knee, 1992). The first lies inside the Herbig Haro object, roughly near knot K position and the second lies westward. Our study of the proper motion does not clarify this uncertainty (Fig. 13, see values in Table 6). THe HH54 knots move roughly in the NNE direction, different from the IRAS 12515-7641 position. Moreover, the inferred outflow inclination angle with respect to the sky ($\sim 15°$), obtained combining both tangential and radial velocities (from Giannini et al., 2005b), indicates that the source should be located firther south than IRAS 12522-7640, where HH54 X and Y are observed, but in this region no other YSOs are detected. Although P.M. analysis does not reveal the driving source, following Knee (1992), we assume that HH54 is the red lobe of the outflow containing HH52 and HH53 and that IRAS 12515-7641 is the exciting source.
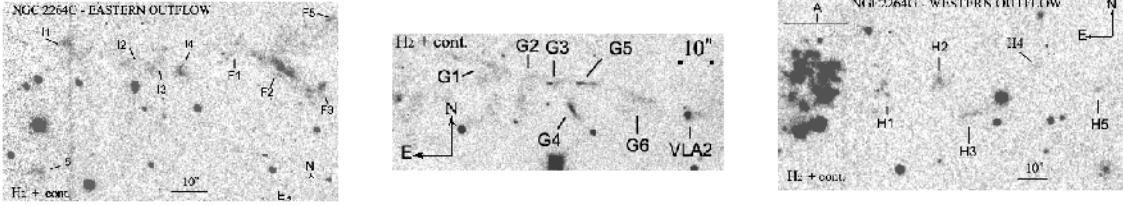
Fig. 11. New detected knots in the NGC2264G outflow (H$_2$ (2.122 μm) image + continuum). **Left:** Knots H in the eastern part of the outflow. **Center:** Knots G in the central part of the outflow. **Right:** Knots H in the western part of the outflow.
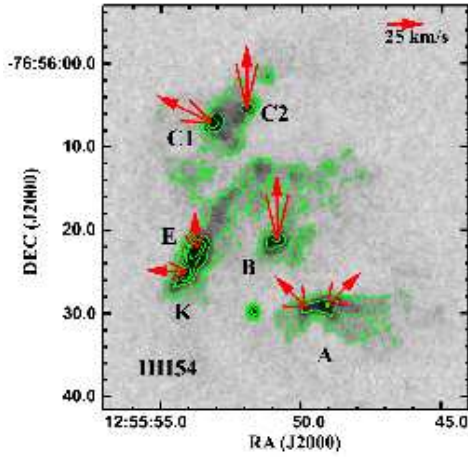
Fig. 13. HH54: H$_2$ (2.122 μm) image (not continuum-subtracted). The arrows show the derived total velocities and the position angles (P.A.) (with their relative errors) of the brightest knots. The contours are 3, 5, 10, 15 and 20× the standard deviation to the mean background (5×10^{-15} erg s^{-1} cm^{-2} arcsec^{-2}).

Table 6. Tangential and total velocities (km s^{-1}), position angles (°) of the studied knots in HH54.

knot	v_{tan} (km s^{-1})	v_{tot} km s^{-1})	P.A. (°)
HH54 A	36±18	37±18	315±31 & 45±31*
HH54 B	50±18	52±18	0±16
HH54 C1	56±18	58±18	63±15
HH54 C2	50±18	52±18	0±16
HH54 E	25±18	28±18	0±31
HH54 K	25±18	28±18	90±20

Notes: * HH54 A has two peaks (estward and westward, see Fig. 13), showing same P.M.s but different P.A.s.

7.10. IRAS18273+0113

*IRAS*18273+0113 (FIRS1 or SMM1, Harvey et al., 1984), in the crowded Serpens star-forming region, powers a bipolar outflow, well traced at NIR wavelengths (e. g. Herbst et al., 1997; Eiroa et al., 1997). In Fig. 14, the H$_2$ image (not continuum-subtracted) shows manifold jets, originated by the several millimetric sources of the region. Following the Herbst et al. (1997) notation, the outflow driven by FIRS1 coincides with knots S5 in the red lobe and with S6 and S7 in the blue lobe. In the H$_2$ continuum-subtracted image (Fig. 14 lower right panel), S5 exhibits a clear bow-shock structure and is followed by another shocked feature labelled S12.

The sub-mm CO studies (Davis et al., 1999) shows that the outflow is much more extended and that knots HH460

(located NW of the source, see Fig. 14 upper left panel) and, possibly, HH459 (Ziener & Eislöffel, 1999; Davis et al., 1999) could be part of it. Probably a deep H$_2$ image of the SE and NW parts of the flow could reveal other molecular emissions.

Conversely, a deep [Fe II] narrow band image does not manifest any iron emission, within an upper limit flux of $F_{1.64\mu m}$=5.3×10^{-16} erg s^{-1} cm^{-2} arcsecs^{-2}.

7.11. R CrA–HH99

R CrA dark cloud is one of the star forming regions closest to the Sun and harbours several YSOs, outflows and HH objects, such as HH99. The exciting source of HH99 is still uncertain. Hartigan et al. (1987) tentatively indicated HH100IR as the driving source of an outflow including HH100 (blue lobe) and HH99 (red lobe). With NIR imaging, Wilking et al. (1997) as well as Davis et al. (1999) suggest IRS 9 or the source R CrA itself. From [S II] large field imaging, Wang et al. (2004) indicate IRS 6 as a possible candidate, but the protostar appears too evolved to have given birth to such a jet (Nisini et al., 2005). Our
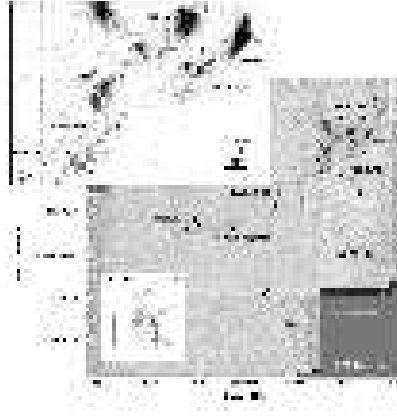
Fig. 12. VLA 1623-243 region: H$_2$ (2.122 μm) image (continuum-subtracted). Inset (upper left corner) is an enlargement of the north-west part of the outflow, showing the tangential velocities and the position angles (P.A.) (with their relative errors) of the brightest knots. The contours are 3, 4, 5, 10 and 20$\times$ the standard deviation to the mean background (8×10^{-15} erg s^{-1} cm^{-2} arcsec^{-2}). In the lower right corner, the tangential velocity and P.A. of HH313 A knots are plotted over their contours (Davis et al., 1999).

proper motion analysis of HH99 (see Fig. 15), obtained from NTT and VLT H$_2$ images (Δt$\sim$6 yr), indicates a P.A. of 39°±6° and tangential velocity of 118±14 km s^{-1} (at a distance of 130 pc), excluding both IRS 6 and 9 as exciting sources. The Class I IRS 7 (here assumed as the driving source) or even a more embedded object of this system (see e.g. Nutter et al., 2004; Hamaguchi et al., 2005) are the best candidates.
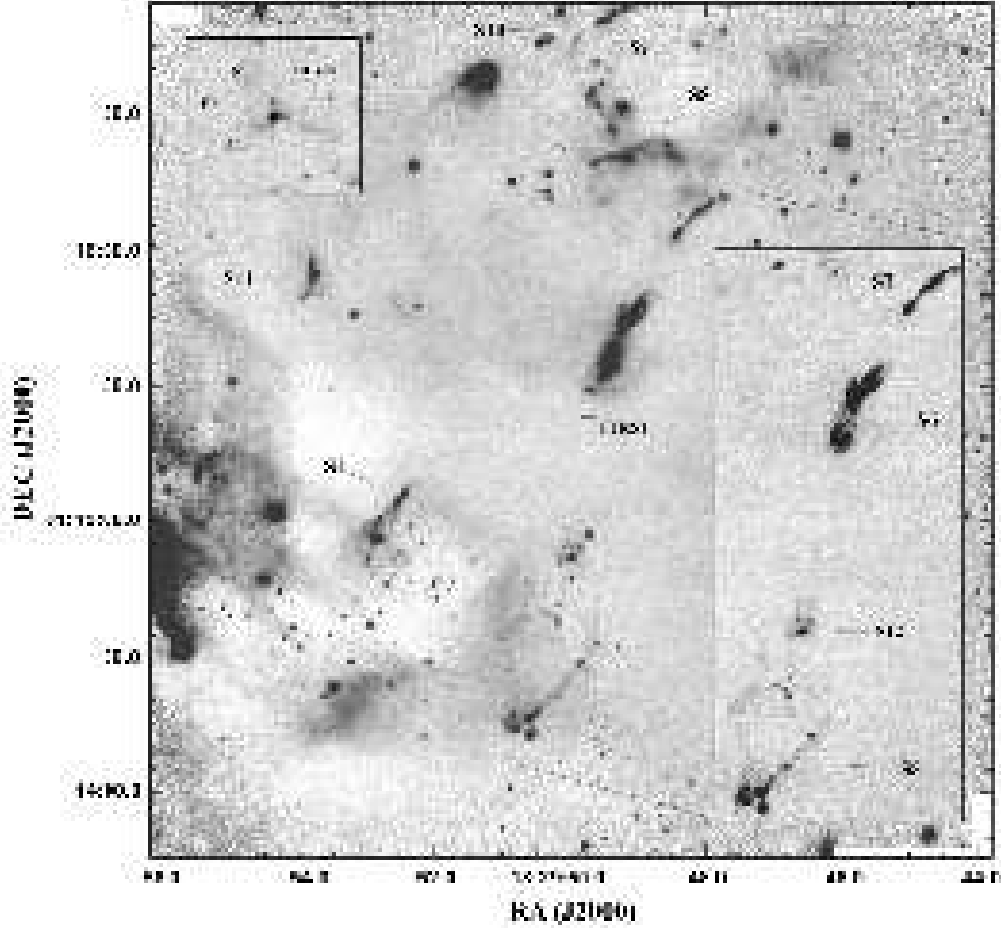
Fig. 14. $IRAS\,18273 + 0113$ region: H_2 ($2.122\,\mu$m) image (not continuum-subtracted) (main picture). On the lower right panel, we show the H_2-K image of the FIRS1 main body outflow, on the upper left the H_2-K image of HH460, located NW outside the main picture and possibly part of the outflow.

7.12. L1157

In our [Fe II] image we detect emission only in the blue lobe outflow. In Fig. 16 (from Davis & Eislöffel, 1995), we show the bright knot A, located in the blue lobe of the outflow, with the iron line (continuum-subtracted) matching the substructures labelled as A1 and 2 in Davis & Eislöffel

(1995), lying on the jet axis with a total measured flux of $F_{1.64\mu m}$=1.1±0.3 $\times 10^{-14}\,\mathrm{erg\,s^{-1}\,cm^{-2}}$.

7.13. IC1396N

$IRAS\,21391 + 5802$ is located inside the bright rimmed globule IC 1369–N in the Cep OB2 association, a very
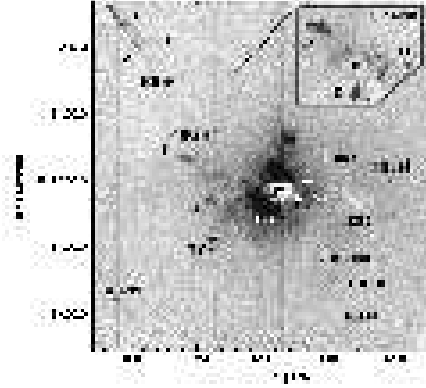
Fig. 15. H$_2$ (2.122 μm) (continuum-subtracted) image of the RCrA region. The arrow shows the tangential velocity and the position angle (P.A.) (with its relative error) of HH99. The newly detected knots (upper right corner) are labelled following Davis et al. (1999).

young and active intermediate mass star-forming region. The region around the IRAS source harbours three YSOs (namely BIMA 1, 2 and 3) (Codella et al., 2001; Beltrán et al., 2002) and the first two generate an outflow.

Fig. 17 (H$_2$ continuum-subtracted image) shows the complex morphology of this region, where at least four outflows can be detected (see Nisini et al., 2001; Reipurth et al., 2003, for details). BIMA 2, the most massive object associated with the IRAS source, gives birth to a spectacular outflow, roughly oriented east–west (Codella et al.,

2001; Beltrán et al., 2002). Knots B, A ,M and HH593 are spatially coincident with the outflow's red lobe, but their location would trace the outflow cavity rather than the jet axis itself. Even if there was a better alignment between the knots and the source, the hypothesis that BIMA 3 has generated knots A and B (Reipurth et al., 2003) seems less likely, because no molecular outflow from the object has been detected in centimetric and millimetric observations (Codella et al., 2001; Beltrán et al., 2002). The blue lobe
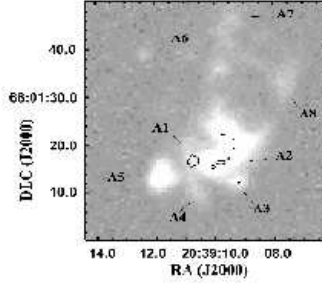
Fig. 16. L1157 knot A: H$_2$ (2.122 μm) image (from Davis & Eislöffel, 1995) with a 3σ [Fe II] (continuum-subtracted) contour.

shows less H$_2$ emission (knots K and Q), possibly because the local extinction is higher.

A strong continuum emission is present in both [Fe II] and H$_2$ images, probably due to the illumination of the nebula by the O6 star HD206267. The 3σ contours in Fig. 17 (superimposed on the 2.12 μm line) show that the [Fe II] emission (continuum-subtracted) mainly originates from knots A and HH593 and near the IRAS source, tracing the higher excited regions. A further [Fe II] detection is observed towards HH777 IRS YSO.
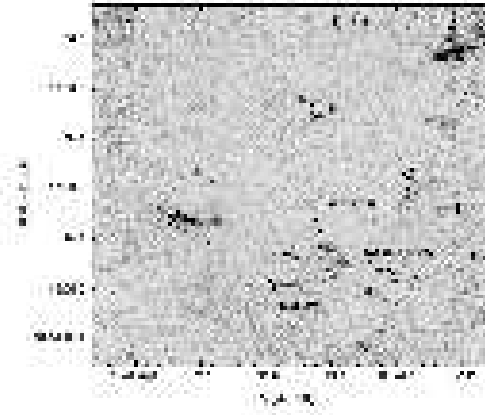
Fig. 17. IRAS21391+5802: H$_2$ (2.122 μm) image (continuum-subtracted) with superimposed 3 and 4 σ [Fe II] contours (white on the H$_2$ emission and black on the background). We label four newly detected knots (N, O, P and Q, see Table 7) in the image, following the nomenclature of Nisini et al. (2001) and Reipurth et al. (2003).

Table 7. H$_2$ (2.122μm) and [Fe II] (1.644μm) fluxes and positions of the new knots detected toward the investigated outflows.

OUTFLOW	KNOT–ID	$F(2.12\mu m) \pm \Delta F$ (10^{-15}erg s^{-1} cm^{-2})	$F(1.64\mu m) \pm \Delta F$ (10^{-15}erg s^{-1} cm^{-2})	α(2000.0) (^{h} ^{m} ^{s})			δ(2000.0) ($^\circ$ $'$ $''$)		
L1448	A-FeII	$\cdots$	3.7±1.2	03	25	38.3	30	44	34.2
L1448	Q–jet	$\cdots$	26±7	03	25	35.7	30	45	19.9
HH211	C	$\cdots$	3±1	03	43	53.4	32	01	14.2
HH211	D	$\cdots$	12±2	03	43	53.9	32	01	04.5
HH211	F	$\cdots$	4.7±0.7	03	43	55.0	32	01	02.7
HH211	I	$\cdots$	11±2	03	43	59.4	32	00	35.0
HH212	NK1	$\cdots$	6.3±1.0	05	43	51.5	-01	02	48.6
HH212	SK1	$\cdots$	5.7±1.0	05	43	51.3	-01	02	58.7
HH212	NB1	$\cdots$	2.8±1.0	05	43	52.3	-01	02	16.2
HH212	SB1	$\cdots$	< 1	05	43	50.3	-01	03	27.3
HH24	A	$\cdots$	20±2	05	46	09.2	-00	10	25.1
HH24	C	$\cdots$	27±3	05	46	00.0	-00	09	51.9
HH24	E	$\cdots$	8±2	05	46	08.6	-00	10	05.7
HH24	D	17±2	$\cdots$	05	46	09.3	-00	09	49.5
HH24	G	44±2	$\cdots$	05	46	11.0	-00	09	22.0
HH24	N	38±2	$\cdots$	05	46	12.0	-00	09	02.0
NGC2264G	G1	2.2±0.4	$\cdots$	06	41	15.3	09	56	14.9
NGC2264G	G2	2.3±0.5	$\cdots$	06	41	14.4	09	56	10.9
NGC2264G	G3	2.4±0.3	$\cdots$	06	41	14.0	09	56	09.2
NGC2264G	G4	5.5±0.3	$\cdots$	06	41	13.5	09	56	00.9
NGC2264G	G5	4.1±0.3	$\cdots$	06	41	13.3	09	56	09.0
NGC2264G	G6	2.8±0.4	$\cdots$	06	41	12.0	09	56	04.2
NGC2264G	H1	4.4±0.4	$\cdots$	06	41	03.8	09	55	53.6
NGC2264G	H2	3.5±0.5	$\cdots$	06	41	02.8	09	55	56.1
NGC2264G	H3	3±1	$\cdots$	06	41	02.2	09	55	46.8
NGC2264G	H4	1.5±0.5	$\cdots$	06	41	01.1	09	55	59.2
NGC2264G	H5	1.5±0.5	$\cdots$	06	41	00.0	09	55	53.5
NGC2264G	I1	6.0±0.5	$\cdots$	06	41	28.1	09	55	53.5
NGC2264G	I2	1.8±0.3	$\cdots$	06	41	27.0	09	55	47.7
NGC2264G	I3	3.5±0.4	$\cdots$	06	41	26.5	09	55	46.4
NGC2264G	I4	5.8±0.3	$\cdots$	06	41	26.0	09	55	45.7
NGC2264G	I5	2.0±0.5	$\cdots$	06	41	28.6	09	55	17.1
VLA1623	GSWC2003–14h	17±4	$\cdots$	16	26	20.6	-24	23	15.6
VLA1623	GSWC2003–14i	4±1	$\cdots$	16	26	19.8	-24	23	19.1
VLA1623	GSWC2003–17b	37±8	$\cdots$	16	26	24.0	-24	24	09.7
OPH–ISO	A	1.6±0.5	$\cdots$	16	26	20.0	-24	24	03.2
OPH–ISO	B	2.0±0.5	$\cdots$	16	26	18.0	-24	24	27.2
IRAS16233	C	17±4	$\cdots$	16	26	25.2	-24	27	34.1
IRAS16233	D	36±8	$\cdots$	16	26	28.4	-24	27	04.3
IRAS18273	S12	5.4±1.0	$\cdots$	18	29	50.2	01	14	51.6
HH593		$\cdots$	13±4	21	40	44.9	+58	16	09.5
IC1396N	A	$\cdots$	21±5	21	40	44.9	+58	16	20.4
IC1396N	N	6.2±0.8	$\cdots$	21	40	47.2	+58	16	01.7
IC1396N	0	4.3±0.9	$\cdots$	21	40	53.5	+58	17	01.6
IC1396N	P	19.8±1.4	$\cdots$	21	40	33.7	+58	17	55.3
IC1396N	Q	10.1±1.5	$\cdots$	21	40	41.7	+58	15	54.2
IC1396N	R	14±2	$\cdots$	21	40	40.2	+58	15	10

Table 8. Physical parameters of the newly observed knots derived through spectroscopy.

knot (object)	Area (10^{-10} sr)[*]	$T(K)$	A_v (mag)	n_e (cm^{-3})
knot 5 (NGC1333I-4A)	3.14	2150±150	8±3	$\cdots$
ASR57 (NGC1333I-4A)	1.86	2650±150	12±3	$\cdots$
i+j (HH211)	7.3	2650±150	8±3	$\cdots$
NB1 (HH212)	1.4	2650±150[b]	4±1	$\cdots$
SB3 (HH212)	2	2650±150[b]	4±1	$\cdots$
NK1 (HH212)	1.36	2800±150[b]	11±2[a]	1.6×10^4
SK1 (HH212)	1.39	2950±180[b]	12±2[a]	10^4-10^5
NK2 (HH212)	0.62	2260±160	12±3	$\cdots$
NK4 (HH212)	0.8	2300±100	12±3	$\cdots$
NK7 (HH212)	0.92	2300±100	12±3	$\cdots$
NB2 (HH212)	1.4	2600±200	8±3	$\cdots$
SK2 (HH212)	0.6	2100±200	12±3	$\cdots$
SK4 (HH212)	0.47	1650±650	12±3	$\cdots$
SK5 (HH212)	0.43	$\cdots$	12±3	$\cdots$
SB2 (HH212)	1.4	2400±200	8±3	$\cdots$
A2 (NGC2264G)	0.68	2500±300	5±3	$\cdots$
A3 (NGC2264G)	0.88	2350±250	5±3	$\cdots$
A7 (NGC2264G)	1.08	2450±350	5±3	$\cdots$
C1 (NGC2264G)	0.75	2500±300	5±3	$\cdots$
C2 (NGC2264G)	0.60	2500±300	5±3	$\cdots$
HH313 A	2.59	3130±130[b]	8±2 12±2[a]	1-6×10^4
HH313 B	3.01	2760±150[b]	8±3	$\cdots$
GSWC2003-13a	2.19	2500±140	8±4	$\cdots$
GSWC2003-13b	1.01	2200±130	8±4	$\cdots$
GSWC2003-14a	1.5	2200±130	8±4	$\cdots$
GSWC2003-14c+14d	4.02	2200±130	8±4	$\cdots$
GSWC2003-14e	1.01	2800±140	8±4	$\cdots$
GSWC2003-14f	1.28	2370±250	8±2	$\cdots$
GSWC2003-14g	1.70	2800±240	8±2	$\cdots$
GSWC2003-14h	3.31	3000±400	8±2	$\cdots$
GSWC2003-18	1.90	2500±300	12±3	$\cdots$
GSWC2003-20b	1.04	2250±300	12±3	$\cdots$
GSWC2003-20c	1.38	2250±300	12±3	$\cdots$
GSWC2003-20d	2	2250±300	12±3	$\cdots$
GSWC2003-20e	0.82	2200±200	12±3	$\cdots$
GSWC2003-20f	1.64	2250±150	12±3	$\cdots$
S6 (serpens)	2.18	2200±200	8±3	$\cdots$
S7 (serpens)	1.71	2600±300	8±3	$\cdots$
A1 (L1157)	1.78	3050±120[b]	< 2	$\cdots$
A2 (L1157)	2.01	3070±140[b]	< 2	$\cdots$
A4 (L1157)	0.76	2090±120	2±1	$\cdots$
A8 (L1157)	0.89	2650±300	2±1	$\cdots$
C1 (L1157)	1.56	2870±130[b]	< 2	$\cdots$
C2 (L1157)	2.20	2600±130[b]	< 2	$\cdots$
C4 (L1157)	1.22	2460±100[b]	2±1	$\cdots$
D3 (L1157)	3.64	2500±300	2±1	$\cdots$
A (IC1396N)	2.88	2740±140	10±5	$\cdots$
B (IC1396N)	1.02	2400±140	10±5	$\cdots$

Notes: [*]Area (length × slit aperture) through which the fluxes in Tables 9-21 have been computed.
Temperature and extinction are derived from H$_2$ lines. We report a label ([a]) when A_v has been obtained from [Fe II].
[b] Knots that show a stratification in temperature. An average T is reported.

Table 9. Observed lines in NGC1333I-4A outflow knots 5 and ASR57

Term	$\lambda(\mu m)$	$F \pm \Delta\,F(10^{-15}\mathrm{erg\,cm^{-2}\,s^{-1}})$	
H$_2$ Lines		knot5	ASR57
1–0 S(9)	1.688	$\cdots$	5.0±0.9
1–0 S(8)	1.715	$\cdots$	3.7±1.0
1–0 S(7)	1.748	7.5±0.7	24.1±0.9
1–0 S(6)	1.788	6.8±1.4	19.5±1.0
1–0 S(3)	1.958	52±5	105±3
2–1 S(4)	2.004	$\cdots$	3.8±1.0
1–0 S(2)	2.034	15.0±1.2	50.0±0.8
3–2 S(5)	2.066	$\cdots$	2.0±0.6
2–1 S(3)	2.073	4.1±1.3	17.8±0.6
1–0 S(1)	2.122	40.6±0.6	130.0±0.6
2–1 S(2)	2.154	$\cdots$	6.8±0.5
3–2 S(3)	2.201	$\cdots$	5.6±0.6
1–0 S(0)	2.223	9.6±0.9	33.5±0.8
2–1 S(1)	2.248	6.6±0.5	18.4±0.7
2–1 S(0)	2.355	$\cdots$	6.0±1.5
3–2 S(1)	2.386	$\cdots$	5.0±1.6
1–0 Q(1)	2.407	43±5	93±5
1–0 Q(2)	2.413	20±5	47±5
1–0 Q(3)	2.424	45±5	84±5
1–0 Q(4)	2.437	$\cdots$	64±5
1–0 Q(5)	2.455	$\cdots$	49±5

Notes: [a]S/N between 2 and 3.

Table 10. Observed lines in HH211 outflow: knots i and j

Term	$\lambda(\mu m)$	$F \pm \Delta\,F(10^{-14}\mathrm{erg\,cm^{-2}\,s^{-1}})$
H$_2$ Lines		I + J
1–0 S(9)	1.688	1.6±0.3
1–0 S(8)	1.715	1.2±0.3
1–0 S(7)	1.748	7.2±0.3
1–0 S(6)	1.788	4.6±0.3
1–0 S(3)	1.958	51±2
2–1 S(4)	2.004	$\cdots$
1–0 S(2)	2.034	13.5±0.3
3–2 S(5)	2.066	0.6±0.3[a]
2–1 S(3)	2.073	3.4±0.3
1–0 S(1)	2.122	35.2±0.3
2–1 S(2)	2.154	2.0±0.3
3–2 S(3)	2.201	1.3±0.3
1–0 S(0)	2.223	7.5±0.3
2–1 S(1)	2.248	3.6±0.3
[Fe II] lines		
[Fe II] $a^4D_{7/2} - a^4F_{9/2}$	1.644	1.1±0.3

Notes: [a]S/N between 2 and 3.

Table 11. Observed lines in HH212 outflow

Term	$\lambda(\mu m)$	$F \pm \Delta\ F(10^{-15}\mathrm{erg\,cm^{-2}\,s^{-1}})$	
H$_2$ Lines		HH212 NB1	HH212 SB3
2–0 S(7)	1.064	2.2±0.6	3±1
2–0 S(5)	1.085	2.2±0.5	2.7±0.6
2–0 S(3)	1.117	$\cdots$	5±1
3–1 S(3)	1.186	1.2±0.4	2.5±0.6
2–0 Q(1)	1.238	1.2±0.3	1.8±0.6
2–0 Q(2)	1.243	0.8±0.2	$\cdots$
2–0 Q(3)	1.247	1.1±0.3	1.5±0.4
2–0 Q(5)	1.263	$\cdots$	2.4±0.8
2–0 Q(7)	1.287	$\cdots$	2.1±0.8[a]
2–0 O(3)	1.335	$\cdots$	2.0±0.4
1–0 S(9)	1.688	1.9±0.3	4.0±0.3
1–0 S(8)	1.715	1.3±0.2	2.8±0.4
1–0 S(7)	1.748	7.8±0.2	13.6±0.4
1–0 S(6)	1.788	7.7±0.8	11.2±0.4
1–0 S(3)	1.958	85±2	$\cdots$
2–1 S(4)	2.004	2.2±0.5	3.8±0.9
1–0 S(2)	2.034	19.7±0.4	23.9±0.9
3–2 S(5)	2.155	$\cdots$	1.2±0.4
2–1 S(3)	2.073	7.1±0.4	9.2±0.5
1–0 S(1)	2.122	48.2±0.7	58.1±0.8
2–1 S(2)	2.154	2.7±0.2	4±2[a]
3–2 S(3)	2.201	1.5±0.4	2.2±0.7
1–0 S(0)	2.223	13.3±0.4	16±1
2–1 S(1)	2.248	8.4±0.4	11.7±0.7
2–1 S(0)	2.356	$\cdots$	3±1
1–0 Q(1)	2.407	76±3	37±8
1–0 Q(2)	2.413	40±4	26±10[a]
1–0 Q(3)	2.424	55±3	$\cdots$
1–0 Q(4)	2.437	39±4	34±7
H$_2$ Lines		HH212 NK1	HH212 SK1
1–0 S(9)	1.688	2.1±0.3	2.6±0.5
1–0 S(8)	1.715	1.8±0.4	2.0±0.3
1–0 S(7)	1.748	8.3±0.4	10.3±0.4
1–0 S(6)	1.788	7.5±0.5	8.7±0.5
1–0 S(3)	1.958	90±3	32±4
2–1 S(4)	2.004	3.5±0.6	6.2±0.5
1–0 S(2)	2.034	27±1	27.1±0.9
2–1 S(3)	2.073	10.8±0.3	15.5±0.8
1–0 S(1)	2.122	62.4±0.5	64.3±0.6
2–1 S(2)	2.154	3.8±0.5	5.0±0.4
3–2 S(3)	2.201	2.6±0.4	3.2±0.5
1–0 S(0)	2.223	18±1	19.4±0.5
2–1 S(1)	2.248	13±1	18.3±0.5
2–1 S(0)	2.356	2.3±0.8	4±1
3–2 S(1)	2.386	3±1	7±2
1–0 Q(1)	2.407	105±3	65±2
1–0 Q(2)	2.413	41±4	39±2
1–0 Q(3)	2.424	76±5	41±2
1–0 Q(4)	2.437	61±5	61±6
1–0 Q(5)	2.455	58±6	120±8
1–0 Q(6)	2.475	$\cdots$	44±10
1–0 Q(7)	2.500	$\cdots$	170±23
[Fe II]	1.257	4.2±0.5	2.5±0.8
[Fe II]	1.534	$\cdots$	1.0±0.3
[Fe II]	1.600	0.8±0.2	0.8±0.2
[Fe II]	1.644	7.7±0.4	6.0±0.4
[Fe II]	1.678	$\cdots$	0.7±0.2

Notes: [a] Signal to noise ratio between 2 and 3.

Table 12. Observed lines in HH212 outflow

Term	$\lambda(\mu m)$	$F \pm \Delta\ F(10^{-15} \mathrm{erg\,cm^{-2}\,s^{-1}})$			
H$_2$ Lines		HH212 NK2	HH212 NK4	HH212 NK7	HH212 NB2
1–0 S(9)	1.688	$\cdots$	$\cdots$	$\cdots$	1.3±0.2
1–0 S(8)	1.715	0.5±0.1	$\cdots$	$\cdots$	0.9±0.2
1–0 S(7)	1.748	1.7±0.4	1.2±0.2	1.7±0.4	4.9±0.2
1–0 S(6)	1.788	1.7±0.5	$\cdots$	$\cdots$	4.9±0.3
1–0 S(3)	1.958	17±1	21±1	17±1	52±1
2–1 S(4)	2.004	$\cdots$	$\cdots$	$\cdots$	1.5±0.3
1–0 S(2)	2.034	6.1±0.4	4.9±0.5	3.4±0.2	11.8±0.6
2–1 S(3)	2.073	2.2±0.4	2.2±0.7	1.2±0.2	4.2±0.4
1–0 S(1)	2.122	13.0±0.5	11.8±0.3	7.4±0.6	25.3±0.3
2–1 S(4)	2.154	0.9±0.2	$\cdots$	0.7±0.2	1.9±0.4
1–0 S(0)	2.223	3.6±0.3	4.1±0.4	3.2±0.9	7.1±0.3
2–1 S(1)	2.248	1.8±0.4	2.9±0.5	1.7±0.7[a]	5.1±0.3
1–0 Q(1)	2.407	23±3	27±2	15±3	44±2
1–0 Q(2)	2.413	11±3	11±2	$\cdots$	20±2
1–0 Q(3)	2.424	$\cdots$	20±2	14±3	36±2
1–0 Q(4)	2.437	$\cdots$	15±3	$\cdots$	19±3
1–0 Q(5)	2.455	$\cdots$	$\cdots$	$\cdots$	21±4

Line	$\lambda(\mu m)$	$F \pm \Delta\ F(10^{-15} \mathrm{erg\,cm^{-2}\,s^{-1}})$				
		HH212 SK2	HH212 SK4	HH212 SK5	HH212 SB1	HH212 SB2
1–0 S(9)	1.688	$\cdots$	$\cdots$	$\cdots$	$\cdots$	1.7±0.6[a]
1–0 S(8)	1.715	$\cdots$	$\cdots$	$\cdots$	$\cdots$	1.1±0.3
1–0 S(7)	1.748	$\cdots$	$\cdots$	$\cdots$	5.3±0.5	6.3±0.4
1–0 S(6)	1.788	$\cdots$	$\cdots$	$\cdots$	3.8±0.5	5.4±0.6
1–0 S(3)	1.958	$\cdots$	$\cdots$	$\cdots$	$\cdots$	9±4[a]
1–0 S(2)	2.034	2.7±0.4	2.1±0.3	$\cdots$	11±2	15.5±0.8
2–1 S(3)	2.073	1.1±0.3	$\cdots$	$\cdots$	3.6±0.6	5.4±0.7
1–0 S(1)	2.122	7.5±0.2	5.1±0.2	1.6±0.2	24.8±0.8	34.0±0.7
2–1 S(2)	2.154	$\cdots$	$\cdots$	$\cdots$	2±1[a]	1.2±0.4
1–0 S(0)	2.223	3.1±0.7	1.5±0.2	$\cdots$	7.9±0.8	9.7±0.5
2–1 S(1)	2.248	1.9±0.4	$\cdots$	$\cdots$	4.6±0.7	7.2±0.6
1–0 Q(1)	2.407	$\cdots$	$\cdots$	$\cdots$	$\cdots$	$\cdots$
1–0 Q(2)	2.413	$\cdots$	$\cdots$	$\cdots$	$\cdots$	$\cdots$
1–0 Q(3)	2.424	$\cdots$	$\cdots$	$\cdots$	$\cdots$	$\cdots$
1–0 Q(4)	2.437	$\cdots$	$\cdots$	$\cdots$	$\cdots$	$\cdots$
1–0 Q(5)	2.455	$\cdots$	$\cdots$	$\cdots$	$\cdots$	$\cdots$

Notes: [a] S/N between 2 and 3.

Table 13. Observed lines in NGC2264G outflow knots A2, A3, A7, C1 and C2

Term	λ(μm)	$F \pm \Delta\ F(10^{-15}\mathrm{erg\,cm^{-2}\,s^{-1}})$				
H$_2$ Lines		A2	A3	A7	C1	C2
1–0 S(9)	1.688	0.8±0.3[a]	⋯	⋯	⋯	⋯
1–0 S(8)	1.715	0.8±0.3[a]	6.7±0.2	⋯	⋯	0.6±0.2
1–0 S(7)	1.748	2.9±0.3	2.8±0.2	1.1±0.3[a]	1.1±0.2	2.9±0.2
1–0 S(6)	1.788	2.2±0.3	2.0±0.2	⋯	0.8±0.3[a]	2.0±0.2
1–0 S(3)	1.958	8.1±1	⋯	5.1±0.4	⋯	20±2
2–1 S(4)	2.004	9.9±0.3	⋯	⋯	⋯	⋯
1–0 S(2)	2.034	5.0±0.2	5.4±0.3	1.7±0.4	1.1±0.3	5.2±0.2
2–1 S(3)	2.073	1.6±0.3	1.6±0.3	⋯	⋯	0.9±0.2
1–0 S(1)	2.122	15.6±0.2	15.8±0.3	4.2±0.4	3.3±0.2	15.5±0.2
2–1 S(2)	2.154	0.8±0.2	1.0±0.2	⋯	0.5±0.2[a]	0.9±0.3
3–2 S(3)	2.201	⋯	0.7±0.3[a]	⋯	⋯	⋯
1–0 S(0)	2.223	4.0±0.2	4.1±0.3	1.1±0.3	0.9±0.2	4.0±0.3
2–1 S(1)	2.248	1.5±0.3	1.5±0.3	1.2±0.3	⋯	1.4±0.3
2–1 S(0)	2.355	0.8±0.3[a]	⋯	⋯	⋯	⋯
3–2 S(1)	2.386	1.1±0.4[a]	1.1±0.4[a]	⋯	⋯	⋯
1–0 Q(1)	2.407	3.8±0.3	4.5±0.5	⋯	⋯	4.5±0.6
1–0 Q(2)	2.413	2.2±0.3	2.1±0.4	⋯	⋯	2.3±0.5
1–0 Q(3)	2.424	3.2±0.3	2.9±0.4	⋯	⋯	3.1±0.5
1–0 Q(4)	2.437	2.8±0.3	4.0±0.4	⋯	⋯	3.8±0.5
1–0 Q(5)	2.455	7.5±0.3	8.3±0.5	⋯	⋯	⋯

Notes: [a]S/N between 2 and 3.

Table 14. Observed lines in VLA1623 HH313 A

Term	$\lambda(\mu m)$	$F \pm \Delta\, F(10^{-15}\mathrm{erg\,cm^{-2}\,s^{-1}})$
H$_2$ Lines		HH313 A
2–0 S(9)	1.053	1.7±0.6[a]
2–0 S(7)	1.064	1.3±0.6[a]
2–0 S(6)	1.073	2.2±0.7
2–0 S(5)	1.085	5.6±1.5
2–0 S(4)	1.100	3.0±1.0
2–0 S(3)	1.117	3.1±0.8
3–1 S(9-10-11)	1.120-1.121	4.3±0.8
3–1 S(7)	1.130	2.7±0.5
2–0 S(2)+3–1 S(6)	1.138-1.140	5.0±1.0
3–1 S(5)	1.152	3.2±0.7
2–0 S(1)	1.162	3.5±0.5
3–1 S(3)	1.186	2.9±0.5
3–1 S(1)	1.233	2.1±0.4
2–0 Q(1)	1.238	3.3±0.5
2–0 Q(2)	1.242	1.4±0.5[a]
2–0 Q(3)	1.247	3.0±0.4
2–0 Q(4)	1.254	1.2±0.4
2–0 Q(5)+3–1 S(0)	1.261-1.263	3.3±0.7
2–0 Q(7)	1.287	2.5±0.3
4–2 S(1)	1.311	1.9±0.6
2–0 O(3)	1.335	3.0±0.3
3–1 Q(5)	1.342	1.9±0.4
5–3 S(3)	1.347	1.2±0.4
1–0 S(11)	1.650	2.7±0.9
1–0 S(10)	1.666	5.6±0.6
1–0 S(9)	1.688	13±1
1–0 S(8)	1.715	9±1
1–0 S(7)	1.748	37±1
1–0 S(6)	1.788	32±1
1–0 S(3)	1.958	38±5
2–1 S(4)	2.004	17±2
1–0 S(2)	2.034	76±1
3–2 S(5)	2.066	3.8±0.6
2–1 S(3)	2.073	22.6±0.5
1–0 S(1)	2.122	215±2
3–2 S(4)	2.127	5±1
2–1 S(2)	2.154	12±1
3–2 S(3)	2.201	5.2±0.9
1–0 S(0)	2.223	41.0±0.8
2–1 S(1)	2.248	21.4±0.8
2–1 S(0)	2.355	8.5±1.2
3–2 S(1)	2.386	7±1
1–0 Q(1)	2.407	193±5
1–0 Q(2)	2.413	97±5
1–0 Q(3)	2.424	213±5
1–0 Q(4)	2.437	76±5
1–0 Q(5)	2.455	116±8
[Fe II] lines	$\lambda(\mu m)$	HH313 A
$a^4D_{7/2} - a^6D_{9/2}$	1.257	5.0±0.4
$a^4D_{7/2} - a^6D_{7/2}$	1.321	3.0±0.6
$a^4D_{5/2} - a^4F_{9/2}$	1.534	5±2[a]
$a^4D_{7/2} - a^4F_{9/2}$	1.644	15±1
$a^4D_{5/2} - a^4F_{7/2}$	1.678	1.0±0.5[a]
Other ionic lines		
[C I] $^1D_2 - {}^3P_2$	0.985	6±1

Notes: [a] S/N ratio between 2 and 3.

Table 15. Observed lines in VLA1623 knots HH313 B, GSWC2003-13a, 13b, 14a, 14c+d, 14e

Term	$\lambda(\mu m)$	$F \pm \Delta\, F(10^{-15} \mathrm{erg\, cm^{-2}\, s^{-1}})$					
H$_2$ Lines		HH313 B	13a	13b	14a	14c+14d	14e
1–0 S(9)	1.688	1.8±0.5	⋯	⋯	⋯	⋯	1.3±0.4
1–0 S(8)	1.715	4.5±0.7	⋯	⋯	⋯	⋯	1.1±0.4[a]
1–0 S(7)	1.748	20.0±0.7	4.9±0.5	⋯	2.5±0.5	3.9±0.5	5.6±0.5
1–0 S(6)	1.788	13.3±0.8	3.7±0.6	⋯	1.9±0.5	2.4±0.9	3.3±0.7
1–0 S(3)	1.958	106±5	34±2	⋯	18±1	30±2	20±2
1–0 S(2)	2.034	45±2	7.9±0.8	⋯	4.4±0.7	7.0±1.0	10.7±0.4
3–2 S(5)	2.066	1.6±0.5	⋯	⋯	⋯	⋯	⋯
2–1 S(3)	2.073	12.7±0.6	2.8±0.4	⋯	1.3±0.6[a]	1.7±0.6[a]	4.6±0.4
1–0 S(1)	2.122	128.0±0.5	19.5±0.4	3.0±0.5	12.1±0.4	18.2±0.6	30.2±0.3
2–1 S(2)	2.154	5.1±0.5	1.4±0.5[a]	⋯	⋯	⋯	2.6±0.3
3–2 S(3)	2.201	3.5±0.4	⋯	⋯	⋯	⋯	1.2±0.3
1–0 S(0)	2.223	30.6±0.6	4.0±0.5	⋯	3.6±0.5	4.1±0.6	7.9±0.3
2–1 S(1)	2.248	14.8±0.6	3.3±0.8	⋯	⋯	2.3±0.8[a]	5.6±0.3
2–1 S(0)	2.355	3.5±1.1	⋯	⋯	⋯	⋯	1.9±0.4
3–2 S(1)	2.386	3.6±1.1	⋯	⋯	⋯	⋯	⋯
1–0 Q(1)	2.407	139±5	21±4	⋯	12±4	19±4	33±2
1–0 Q(2)	2.413	57±5	⋯	⋯	⋯	⋯	12±2
1–0 Q(3)	2.424	140±5	19±4	⋯	12±4	18±4	33±2
1–0 Q(4)	2.437	45±5	⋯	⋯	⋯	⋯	10±2
1–0 Q(5)	2.455	41±5	⋯	⋯	⋯	⋯	14±2

Notes: [a] S/N between 2 and 3.

Table 16. Observed lines in VLA1623 knots GSWC2003-14f, 14g, 14h, 18, 20b, 20c, 20d

H$_2$ Lines		14f	14g	14h	18	20b	20c	20d
1–0 S(7)	1.748	2.2±0.6	10.3±0.9	4.0±1.0	⋯	⋯	7.4±0.5	4.8±0.5
1–0 S(6)	1.788	⋯	9.0±0.8	4.6±1.5	1.7±0.6[a]	⋯	6.1±0.6	4.3±0.6
1–0 S(3)	1.958	⋯	19.3±3	⋯	10±2	⋯	8±2	27±4
1–0 S(2)	2.034	2.7±0.7	13.3±0.6	5.0±1.0	3.8±0.5	1.4±0.5[a]	5.7±0.6	9.6±0.6
2–1 S(3)	2.073	⋯	6.8±0.9	⋯	2.0±0.6	⋯	1.7±0.6[a]	5.7±0.6
1–0 S(1)	2.122	10.3±0.3	43.2±0.5	17±1	11.9±0.8	3.2±0.4	13.0±0.8	34.5±0.8
2–1 S(2)	2.154	⋯	4.1±0.7	1.7±0.7[a]	⋯	⋯	⋯	2.1±0.5
3–2 S(3)	2.201	⋯	2.2±0.9[a]	⋯	⋯	⋯	⋯	1.4±0.4
1–0 S(0)	2.223	2.2±0.4	10.3±0.4	5.0±1.0	4.4±0.8	⋯	3.8±0.5	9.0±0.7
2–1 S(1)	2.248	1.6±0.5	8.9±0.6	4±1	2.4±0.8	1.6±0.5	⋯	4.1±0.7
1–0 Q(1)	2.407	13±2	48±2	4±1	17±2	⋯	17±4	37±4
1–0 Q(2)	2.413	⋯	24±2	⋯	4±2[a]	⋯	6±2	15±4
1–0 Q(3)	2.424	13±2	55±2	⋯	18±2	⋯	19±3	41±4
1–0 Q(4)	2.437	⋯	25±5	⋯	6±3	⋯	⋯	10±4[a]
1–0 Q(5)	2.455	⋯	32±5	⋯	15±4	⋯	13±5	27±5

Notes: [a] S/N between 2 and 3.

Table 17. Observed lines in VLA1623 knots GSWC2003-20e, 20f

H$_2$ Lines		20e	20f
1–0 S(9)	1.688	$\cdots$	1.7±0.7[a]
1–0 S(8)	1.715	$\cdots$	$\cdots$
1–0 S(7)	1.748	1.3±0.5[a]	4.8±0.7
1–0 S(6)	1.788	1.3±0.5[a]	4.1±0.8
1–0 S(3)	1.958	5±2[a]	10±2
1–0 S(2)	2.034	2.6±0.5	16.7±0.6
3–2 S(5)	2.066	$\cdots$	$\cdots$
2–1 S(3)	2.073	0.8±0.3[a]	5.1±0.6
1–0 S(1)	2.122	7.7±0.4	46.0±0.5
2–1 S(2)	2.154	$\cdots$	1.9±0.4
3–2 S(3)	2.201	$\cdots$	1.0±0.4[a]
1–0 S(0)	2.223	1.9±0.5	13.6±0.6
2–1 S(1)	2.248	$\cdots$	5.4±0.6
2–1 S(0)	2.355	$\cdots$	$\cdots$
3–2 S(1)	2.386	$\cdots$	$\cdots$
1–0 Q(1)	2.407	8±2	59±5
1–0 Q(2)	2.413	4±2[a]	23±5
1–0 Q(3)	2.424	10±2	58±5
1–0 Q(4)	2.437	$\cdots$	20±5
1–0 Q(5)	2.455	7±2	32±5

Notes: [a]S/N between 2 and 3.

Table 18. [Fe II] observed lines in knots HH313 B, GSWC2003-14g, 14h

Line	$\lambda(\mu m)$	$F \pm \Delta\ F(10^{-15}\ \mathrm{erg\,cm^{-2}\,s^{-1}})$		
[Fe II] lines		HH313 B	14g	14h
$a^4D_{7/2} - a^6D_{9/2}$	1.257	$\cdots$	1.4±0.6[a]	1.5±0.5
$a^4D_{7/2} - a^4F_{9/2}$	1.644	1.8±0.5	6.0±0.7	7.2±0.5

Notes:[a]S/N between 2 and 3.

Table 19. Observed lines in IRAS18273+0113 outflow knots S6 and S7

Term	$\lambda(\mu m)$	$F \pm \Delta\ F(10^{-15}\mathrm{erg\,cm^{-2}\,s^{-1}})$	
H$_2$ Lines		S6	S7
1–0 S(7)	1.748	3.3±0.7	$\cdots$
1–0 S(6)	1.788	3.4±0.8	2.8±0.8
1–0 S(3)	1.958	37±2	17±1
1–0 S(2)	2.034	14.9±1.2	7±1
2–1 S(3)	2.073	3.2±0.6	2.9±0.5
1–0 S(1)	2.122	41.1±0.5	14.8±0.3
2–1 S(4)	2.154	1.3±0.3	$\cdots$
1–0 S(0)	2.223	11.1±0.7	5.2±0.8
2–1 S(1)	2.248	5.3±0.4	2.8±0.6
2–1 S(0)	2.355	1.1±0.3	$\cdots$
1–0 Q(1)	2.407	37±2	14±1
1–0 Q(2)	2.413	15±2	5±1
1–0 Q(3)	2.424	35±2	11±1
1–0 Q(4)	2.437	9±1	$\cdots$
1–0 Q(5)	2.455	9±1	$\cdots$

Notes: [a]S/N between 2 and 3.

Table 20. Observed lines in L1157 knots A1, A2, C1, C2 and C4

Term	$\lambda(\mu m)$	$F \pm \Delta\ F(10^{-15}\mathrm{erg\,cm^{-2}\,s^{-1}})$				
H$_2$ Lines		A1	A2	C1	C2	C4
2–0 S(4)	1.100	2.4±0.4	2.5±0.8	⋯	⋯	⋯
2–0 S(3)	1.117	7.8±0.8	6.0±2.0	⋯	⋯	⋯
3–1 S(7)	1.130	2.5±0.8	⋯	⋯	⋯	⋯
2–0 S(2)+3–1 S(6)	1.138-1.140	4.4±2.0^a	⋯	⋯	⋯	⋯
3–1 S(5)	1.152	5.0±1.0	2.9±0.9	3.3±1.1	⋯	⋯
2–0 S(1)	1.162	4.9±1.5	3.4±0.5	6.4±2.0	5.3±1.5	1.7±0.5
3–1 S(3)	1.186	3.6±0.6	2.3±0.5	2.3±1.0^a	⋯	⋯
4–2 S(9)	1.196	1.3±0.4	1.0±0.5^a	⋯	⋯	⋯
4–2 S(7)+3–1 S(2)	1.205-1.207	1.2±0.5^a	2.0±0.6	⋯	⋯	⋯
4–2 S(5)	1.226	1.8±0.5	1.8±0.5	2.1±0.8^a	⋯	⋯
3–1 S(1)	1.233	2.6±0.6	2.3±0.5	1.6±0.8^a	⋯	⋯
2–0 Q(1)	1.238	4.0±0.6	2.1±0.4	4±1	4.8±1.5	1.2±0.4
2–0 Q(2)	1.242	2.8±0.5	1.3±0.4	⋯	⋯	⋯
2–0 Q(3)	1.247	3.2±0.4	2.3±0.4	5±1	3±1	1±0.4^a
2–0 Q(4)	1.254	2.1±0.5	1.0±0.4^a	1.6±0.6^a	⋯	⋯
4–2 S(3)+2–0 Q(5)+3–1 S(0)	1.261-1.263	3.8±0.5	3.8±0.5	3.2±1.0	⋯	⋯
4–2 S(2)+2–0 Q(7)	1.285-1.287	3.4±0.7	1.5±0.5	3.3±1.0	⋯	⋯
4–2 S(1)	1.311	1.4±0.3	2.5±0.8	1.9±0.9^a	⋯	⋯
3–1 Q(1)	1.314	2.4±0.4	⋯	⋯	⋯	⋯
2–0 Q(9)	1.319	2.8±0.8	1.8±0.6	2.6±0.9^a	⋯	⋯
3–1 Q(3)	1.324	1.6±0.8^a	⋯	⋯	⋯	⋯
2–0 O(3)	1.335	2.7±0.7	2.3±0.6	2.7±0.9	⋯	⋯
3–1 Q(5)+4–2 S(0)	1.342-1.342	2.3±0.7	1.7±0.7^a	1.5±0.9^a	⋯	⋯
5–3 S(3)	1.347	1.4±0.7^a	2±1^a	⋯	⋯	⋯
1–0 S(11)	1.650	1.1±0.4^a	1.2±0.4	⋯	⋯	⋯
1–0 S(9)	1.688	4.3±0.8	4.3±0.5	4.4±0.8	3.5±0.8	1.4±0.4
1–0 S(8)	1.715	4.1±0.8	3.4±0.8	4.2±0.9	5.1±0.7	1.0±0.4^a
1–0 S(7)	1.748	16.7±0.8	14.2±0.6	13.3±0.9	15.6±0.5	4.3±0.5
1–0 S(6)	1.788	13.0±0.8	10.3±0.8	9.6±0.7	10.6±0.5	3.2±0.7
1–0 S(5)	1.835^b	106±20	98±23	⋯	⋯	⋯
1–0 S(4)	1.891^b	105±20	88±16	⋯	⋯	⋯
1–0 S(3)	1.958	136±5	132±16	73±5	87±5	20±5
2–1 S(4)	2.004	4.6±0.7	2.7±0.7	⋯	⋯	⋯
1–0 S(2)	2.034	21.0±0.4	15.9±0.9	17.0±0.6	19.7±0.8	6.0±0.8
3–2 S(5)	2.066	1.6±0.3	1.9±0.4	⋯	⋯	⋯
2–1 S(3)	2.073	6.2±0.4	6.2±0.5	6.0±0.5	7.8±0.8	1.8±0.5
1–0 S(1)	2.122	52.6±0.6	40.2±0.5	44.6±0.4	53.6±0.5	13.8±0.3
2–1 S(2)	2.154	2.4±0.4	2.1±0.3	2.0±0.4	2.2±0.5	0.9±0.3
3–2 S(3)	2.201	1.3±0.3	2.5±0.3	1.3±0.6^a	1.9±0.3	⋯
1–0 S(0)	2.223	12.1±0.4	9.6±0.5	10.3±0.5	12.4±0.3	3.4±0.3
2–1 S(1)	2.248	6.6±0.5	6.7±0.5	5.1±0.5	6.3±0.6	1.9±0.4
2–1 S(0)	2.355	1.6±0.8^a	2.5±0.8	⋯	2.1±0.7	⋯
3–2 S(1)	2.386	1.4±0.6^a	1.8±0.6	⋯	2.3±0.8^a	⋯
1–0 Q(1)	2.407	58±5	41±5	37±5	49±5	13±3
1–0 Q(2)	2.413	24±5	14±5	14±5	21±5	⋯
1–0 Q(3)	2.424	53±5	39±5	30±5	39±5	11±3
1–0 Q(4)	2.437	27±5	19±5	14±5	18±5	⋯
1–0 Q(5)	2.455	27±5	19±5	10±5^a	⋯	⋯
[Fe II] lines						
$a^4D_{7/2} - a^6D_{9/2}$	1.257	0.5±0.2^a	3.6±0.5	⋯	⋯	⋯
$a^4D_{7/2} - a^4F_{9/2}$	1.644	0.6±0.3^a	3.8±0.6	⋯	⋯	⋯

Notes: ^{a}S/N between 2 and 3.

Table 21. Observed lines in L1157 knots A4, A8 and D3

Term	$\lambda(\mu m)$	$F \pm \Delta\, F(10^{-15} \mathrm{erg\,cm^{-2}\,s^{-1}})$		
H$_2$ Lines		A4	A8	D3
1–0 S(7)	1.748	1.5±0.3	1.4±0.4	3.1±0.9
1–0 S(6)	1.788	1.3±0.3	⋯	3.3±1.0
1–0 S(3)	1.958	28±5	10±3	30±5
1–0 S(2)	2.034	3.8±0.4	1.3±0.4	5.8±0.7
2–1 S(3)	2.073	0.8±0.3^a	⋯	2.5±0.7
1–0 S(1)	2.122	7.7±0.3	3.2±0.4	12.0±0.4
2–1 S(2)	2.154	0.6±0.3^a	⋯	0.6±0.3^a
1–0 S(0)	2.223	2.5±0.4	0.9±0.3	2.7±0.5
2–1 S(1)	2.248	0.8±0.3^a	⋯	⋯
1–0 Q(1)	2.407	9±3	⋯	13±4
1–0 Q(3)	2.424	8±3	⋯	8±4^a

Notes: ^{a}S/N between 2 and 3.

Table 22. Observed lines in IC1396N outflow knots A and B

Term	$\lambda(\mu m)$	$F \pm \Delta\, F(10^{-15} \mathrm{erg\,cm^{-2}\,s^{-1}})$	
H$_2$ Lines		A	B
1–0 S(9)	1.688	1.5±0.3	⋯
1–0 S(7)	1.748	3.2±0.3	1.6±0.3
1–0 S(6)	1.788	3.2±0.4	1.4±0.4
1–0 S(3)	1.958	33±3	13±1
2–1 S(4)	2.004	1.2±0.4	⋯
1–0 S(2)	2.034	6.5±0.4	3.6±0.4
2–1 S(3)	2.073	1.0±0.3	⋯
1–0 S(1)	2.122	17.3±0.3	9.1±0.4
2–1 S(2)	2.154	1.0±0.3	⋯
3–2 S(3)	2.201	0.7±0.3^a	⋯
1–0 S(0)	2.223	4.2±0.3	2.4±0.3
1–0 Q(1)	2.407	19±2	11±2
1–0 Q(2)	2.413	8±2	⋯
1–0 Q(3)	2.424	18±2	9±2
Atomic and Ionic lines			
[Fe II] $a^4D_{7/2} - a^4F_{9/2}$	1.644	2.3±0.4	⋯

Notes: ^{a}S/N between 2 and 3.